

# Vertical structures induced by embedded moonlets in Saturn's rings



Holger Hoffmann<sup>a,\*</sup>, Martin Seiß<sup>a</sup>, Heikki Salo<sup>b</sup>, Frank Spahn<sup>a</sup>

<sup>a</sup> Institute of Physics and Astronomy, University of Potsdam, 14476 Golm, Germany

<sup>b</sup> Division of Astronomy, Department of Physics, University of Oulu, PL 3000, FI-90014, Finland

## ARTICLE INFO

### Article history:

Received 27 August 2014

Revised 8 December 2014

Accepted 2 February 2015

Available online 11 February 2015

### Keywords:

Planetary rings

Saturn, rings

Saturn, satellites

Disks

## ABSTRACT

We study the vertical extent of propeller structures in Saturn's rings (i) by extending the model of Spahn and Sremčević (Spahn, F., Sremčević, M. [2000]. *Astron. Astrophys.*, 358, 368–372) to include the vertical direction and (ii) by performing N-body box simulations of a perturbing moonlet embedded into the rings. We find that the gravitational interaction of ring particles with a non-inclined moonlet does not induce considerable vertical excursions of ring particles, but causes a considerable thermal motion in the ring plane. We expect ring particle collisions to partly convert the lateral induced thermal motion into vertical excursions of ring particles in the course of a quasi-thermalization. The N-body box simulations lead to maximal propeller heights of about 0.6–0.8 Hill radii of the embedded perturbing moonlet. Moonlet sizes estimated by this relation are in good agreement with size estimates from radial propeller scalings for the propellers Blériot and Earhart. For large propellers, the extended hydrodynamical propeller model predicts an exponential propeller height relaxation, confirmed by N-body box simulations of non-self gravitating ring particles. Exponential cooling constants, calculated from the hydrodynamical propeller model agree fairly well with values from fits to the tail of the azimuthal height decay of the N-body box simulations. From exponential cooling constants, determined from shadows cast by the propeller Earhart and imaged by the Cassini spacecraft, we estimate collision frequencies of about 6 collisions per particle per orbit in the propeller gap region and about 11 collisions per particle per orbit in the propeller wake region.

© 2015 Elsevier Inc. All rights reserved.

## 1. Introduction

Planetary rings are one of the most remarkable and beautiful cosmic structures. They are natural dynamical laboratories (Burns and Cuzzi, 2006), exemplifying the physics of cosmic disks, such as accretion or galactic disks, which are much larger and much farther away from Earth. An exciting example is the presence of small moons embedded in Saturn's rings, henceforth called moonlets, which have their analog in planetary embryos orbiting within a protoplanetary disk (Artymowicz, 2006; Papaloizou, 2007).

The fact that spacecraft cameras (even Cassini's) do not have sufficient resolution to image these moonlets directly, brought up the idea of investigating moonlet-induced putative structures in the rings (Lissauer et al., 1981; Henon, 1981; Spahn, 1987; Petit and Henon, 1988; Spahn and Wiebicke, 1989), with the hope that these features could be captured by the spacecraft cameras or instruments. This then led to predictions of 'propeller'-shaped

structures (Spahn and Sremčević, 2000; Sremčević et al., 2002) which are carved in the rings by the moonlet. Subsequent numerical particle experiments (Seiß et al., 2005; Sremčević et al., 2007; Lewis and Stewart, 2009) clarified the fingerprint of such gravitational perturbers and confirmed the spatial scaling of the propeller structure. Depending on its size, an embedded ring-moon either induces a partial gap (sizes below a few km) or, alternatively, opens up a complete circumferential gap (for sizes above a few km, e.g. the ring-moons *Pan* and *Daphnis*). Both structures are decorated with density wakes, completing the structural picture. Up to this stage, analytical study of propellers has focused exclusively on structure within the ring plane.

More than 150 propellers have now been detected (Tiscareno et al., 2006; Tiscareno et al., 2008; Sremčević et al., 2007) and among them a few which are large enough to be seen on several snapshots taken by Cassini's cameras at different times, confirming in this way their orbital motion. Those propellers were nicknamed after famous aviators, e.g.: Blériot, Kingsford Smith, Earhart (Tiscareno et al., 2010).

In the summer of 2009, at Saturn's equinox (the sunset at Saturn's rings), the perfect opportunity arose to detect any vertical

\* Corresponding author.

E-mail address: [hohoff@uni-potsdam.de](mailto:hohoff@uni-potsdam.de) (H. Hoffmann).

structure deviating from the mean ring plane by observing shadows cast on the rings. At this time the density structures around the largest propeller moonlets, as well as those around the ring-moon *Daphnis*, created prominent shadows. These can be assigned to the wakes and in the case of the propeller moonlets also to excited regions of the propeller, where the moonlet induces two partial gaps. The shadows were much longer than the moon's size itself, leading to the conclusion that moonlet-induced vertical excursions of ring particles can be in the range of several kilometers in the case of *Daphnis* or several hundred meters in the case of the large propeller moonlets. These very facts directly indicate the necessity to investigate the vertical stratification of moonlet-induced structures, which has not been the focus of former models of the moonlet's *fingerprint*.

Our study of the vertical extend of moonlet-induced propeller structures is organized as follows: In Section 2 the extended hydrodynamical propeller model is presented. In Section 2.2 we calculate the mass flow through the scattering region by a probabilistic approach and determine values of the moonlet-induced thermal velocities, which we use later as initial conditions for the hydrodynamical equations describing the long term relaxation of the moonlet-excited structures. Section 2.3 gives the hydrodynamical balance equations, which we use to model the diffusion of mass into the induced gap and the relaxation of the granular ring temperature. In Section 3 the azimuthal relaxation of the propeller height is calculated. Section 4 describes N-body box simulations of propeller moonlets embedded into the rings. These are used to verify assumptions made in the derivation of the extended propeller model and to compare results. Finally, we present and discuss the application of our results to observed propeller features in Saturn's rings in Section 5.

## 2. Extended model of gravitational scattering

### 2.1. The scattering region

The first step in the formulation of our model is to divide the planetary ring, composed of the ring particles and one moonlet, into two regions:

- (i) the rather small scattering region,
- (ii) the rest of the ring.

In this work we consider moonlets on circular and planar orbits, i.e. with zero eccentricity and zero inclination. The scattering region is the small area (volume) around the moonlet where trajectory changes due to the moonlet's gravity predominantly take place. This region of the embedded moonlet's gravitational influence is of the order of a few times the Hill radius

$$h = a_0 \left( \frac{m_m}{3(m_m + m_s)} \right)^{1/3}, \quad (1)$$

where  $a_0$  is the semimajor axis of the moonlet,  $m_m$  its mass and  $m_s$  the mass of Saturn. Compared to the moonlet's semimajor axis the Hill radius is usually very small. For large propellers, like Blériot or Earhart, the ratio  $h^* = h/a_0$  is approximately  $10^{-6}$  (Tiscareno et al., 2010). This low ratio naturally allows the splitting of the rings into the two regions, and further, it allows to regard the azimuthal extent of the scattering region to be zero, i.e. the approximation of the scattering region by a scattering line (Spahn and Wiebicke, 1989).

For the rest of the ring, where the moonlet's gravity is negligible, the moonlet-induced structures are assumed to relax due to inelastic collisional cooling and viscous diffusion (Spahn and Sremčević, 2000; Sremčević et al., 2002). The ring is regarded as a fluid and described with hydrodynamical balance equations,

where the granular temperature<sup>1</sup>  $T = c^2/3$  is used to describe the energy balance of the ring (Schmidt et al., 2009) and  $c$  denotes the velocity dispersion of the ring particles.

### 2.2. Encounter with the moonlet – gravitational scattering

We describe the encounter of ring particles with the moonlet in a corotating frame, rotating about Saturn with the Keplerian frequency  $\Omega_0 = (Gm_s/a_0^3)^{1/2}$  of the moonlet. The dynamics of ring particles in the corotating frame is given by the equation

$$\ddot{\mathbf{r}} + 2\boldsymbol{\Omega}_0 \times \dot{\mathbf{r}} + \boldsymbol{\Omega}_0 \times (\boldsymbol{\Omega}_0 \times \mathbf{r}) = -\nabla\Phi_s - \nabla\Phi_m, \quad (2)$$

where  $\mathbf{r}$  is the position vector of the ring particle relative to Saturn's center,  $\boldsymbol{\Omega}_0$  is aligned with the planetocentric angular momentum of the moonlet and has magnitude  $\Omega_0$ , and  $\Phi_s$  and  $\Phi_m$  are the gravitational potentials due to Saturn and the moonlet (assumed to be point masses,  $\Phi_s = -Gm_s/r$ ,  $\Phi_m = -Gm_m/s$ , where  $s$  denotes the distance of the ring particle to the moonlet).

Hereby, for simplicity, we neglect Saturn's oblateness, which would result in slightly different mean motion, epicyclic frequency and vertical frequency (less than one percent difference for the semimajor axis of Earhart, respectively). It would also result in a moving pericenter and ascending node of the ring particle orbits, effects, which would be averaged-out in the calculation of the scattering operator in Section 2.2.2.

The ring particles are on orbits with low eccentricity and inclination and the mass of the moonlet is very small compared to Saturn's mass  $m_m/m_s \ll 1$ . Because we are interested in the ring particle motion in the vicinity of the moonlet, we fix the origin of the corotating frame to the mean orbital location of the moonlet. In the vicinity of the moonlet the equations of motion of ring particles are well approximated by Hill's equations (Hill, 1878; Hénon and Petit, 1986).

We assume that the  $x$  axis points radially outward, the  $y$  axis points into the azimuthal direction in which the moonlet is moving and the  $z$  axis is normal to the ring plane in such a way that the axes form a right-handed coordinate system. With the scaled coordinates  $\tilde{x} = x/h$ ,  $\tilde{y} = y/h$ ,  $\tilde{z} = z/h$  and scaled time  $t' = \Omega_0 t$ , Hill's equations then read

$$\begin{aligned} \ddot{\tilde{x}} &= 2\dot{\tilde{y}} + 3\tilde{x} - 3\tilde{x}/\tilde{s}^3 \\ \ddot{\tilde{y}} &= -2\dot{\tilde{x}} - 3\tilde{y}/\tilde{s}^3 \\ \ddot{\tilde{z}} &= -\tilde{z} - 3\tilde{z}/\tilde{s}^3, \end{aligned} \quad (3)$$

where  $\tilde{s}^2 = \tilde{x}^2 + \tilde{y}^2 + \tilde{z}^2$  is the scaled distance of the ring particle to the moonlet and  $\dot{\tilde{x}} = d\tilde{x}/dt'$ . These equations are point symmetric about the position of the moonlet ( $\tilde{x} = \tilde{y} = \tilde{z} = 0$ ), and quite comfortably, they do not depend on the moonlet mass anymore. All information of the moonlet mass is contained in the scaling length  $h$ .

When the ring particles are not in the vicinity of the moonlet, i.e.  $1/\tilde{s}^3 \rightarrow 0$  and therefore  $|\nabla\Phi_m| \rightarrow 0$ , their trajectories are well described by the solutions to the homogeneous Hill's equations

$$\begin{aligned} \tilde{x}(t') &= \tilde{a} - \tilde{e} \cos(t' + \psi) \\ \tilde{y}(t') &= C - \frac{3}{2}\tilde{a}t' + 2\tilde{e} \sin(t' + \psi) \\ \tilde{z}(t') &= \tilde{i} \sin(t' + \zeta). \end{aligned} \quad (4)$$

The semimajor axis, eccentricity and inclination are scaled according to

<sup>1</sup> The granular temperature is a measure of the random motion of the (macroscopic) ring particles and should not be confused with the thermodynamic temperature.

$$\tilde{a} = \frac{a - a_0}{h}, \quad \tilde{e} = \frac{ea_0}{h}, \quad \tilde{i} = \frac{ia_0}{h}. \quad (5)$$

The phases  $\psi$  and  $\zeta$  are the longitude of pericenter and the longitude of the ascending node, respectively.

### 2.2.1. Test particle integrations

In order to quantify the action of the moonlet gravity on the ring particles, we integrate the equations of motion numerically for a set of test particles using a 5th order embedded Runge–Kutta scheme with adaptive step size control (Press et al., 1992). The moonlet and Saturn are assumed to be point masses. The integrations start upstream of the moonlet at an azimuthal distance of 1000 Hill radii to the moonlet and are terminated when the test particle's downstream azimuthal distance exceeds 1000 Hill radii. These limits ensure that the region of interaction is well characterized by the integrations.

We take the initial semimajor axis of the test particles to be uniformly distributed in the range of  $-20$  to  $20$  Hill radii radial distance to the moonlet. The initial eccentricities and inclinations of the test particles are chosen to be Rayleigh distributed

$$f(\tilde{e}, \tilde{i}) = \frac{\tilde{e}}{\tilde{c}_x^2} \exp\left(-\frac{\tilde{e}^2}{2\tilde{c}_x^2}\right) \frac{\tilde{i}}{\tilde{c}_z^2} \exp\left(-\frac{\tilde{i}^2}{2\tilde{c}_z^2}\right), \quad (6)$$

with uniformly distributed initial phases  $\psi$  and  $\zeta$ . This is a fair assumption for many kinds of disks (Petit and Hénon, 1987; Ida and Makino, 1992; Lissauer, 1993; Ohtsuki and Emori, 2000; Sremčević et al., 2002).

This distribution of orbital elements corresponds to a triaxial Gaussian velocity distribution

$$f(\tilde{v}_x, \tilde{v}_y, \tilde{v}_z) = \frac{1}{\pi\tilde{c}_x^2} \exp\left(-\frac{\tilde{v}_x^2 + 4\tilde{v}_y^2}{2\tilde{c}_x^2}\right) \frac{1}{\sqrt{2\pi}\tilde{c}_z} \exp\left(-\frac{\tilde{v}_z^2}{2\tilde{c}_z^2}\right) \quad (7)$$

with a diagonal velocity dispersion tensor  $\mathbf{T}$ , where  $T_{xx} = \tilde{c}_x^2$ ,  $T_{yy} = (\tilde{c}_x/2)^2$  and  $T_{zz} = \tilde{c}_z^2$ . The scaled quantities  $\tilde{c}_x$ ,  $\tilde{c}_z$  are related to the unscaled ones by

$$\tilde{c}_x = c_x/(\Omega_0 h), \quad \tilde{c}_z = c_z/(\Omega_0 h). \quad (8)$$

We choose the quasi-equilibrium ratio for thermal velocities in the dense rings  $(\tilde{c}_z/\tilde{c}_x)_{\text{eq}} = 0.65$ , which is consistent with the above triaxial Gaussian velocity distribution (Goldreich and Tremaine, 1978) and which is a reasonable value if self-gravity is neglected (Salo et al., 2001).

During the trajectory integrations, the test particles, the moonlet and Saturn are assumed to be point masses and the minimal distance of the test particles to the moonlet is recorded. For simplicity, we ignored particles which would collide with a spherical moonlet of finite size in further calculations. However, we also performed numerical calculations with a finite moonlet size and found no significant influence on the results discussed here.

### 2.2.2. Mass transfer

We use the approach of Spahn and Wiebicke (1989) to describe the mass transfer through the scattering region. Motivated by the chaotic behavior of single particle trajectories near the moonlet (Petit and Hénon, 1986), the encounter of ring particles with the moonlet is modeled by a probabilistic Markov chain model. The results of the test particle integrations are used to calculate transitional probabilities between initial  $(\tilde{x}, \tilde{z})$  and final  $(\tilde{x}', \tilde{z}')$  positions of the test particles at the azimuthal boundary of the scattering region.

These probabilities define a scattering operator  $A$ , where  $A(\tilde{x}', \tilde{z}' | \tilde{x}, \tilde{z}) d\tilde{x} d\tilde{z}$  is the probability that matter is scattered from  $(\tilde{x}, \tilde{x} + d\tilde{x}) \times (\tilde{z}, \tilde{z} + d\tilde{z})$  to  $(\tilde{x}', \tilde{x}' + d\tilde{x}') \times (\tilde{z}', \tilde{z}' + d\tilde{z}')$ . The primes denote values after the scattering.

We assume that the scattering region can be approximated by the  $\tilde{x}$ – $\tilde{z}$  plane at  $\tilde{y} = 0$ , which connects Saturn and the moonlet and is analogous to the scattering line as defined in Spahn and Wiebicke (1989). In our model, the complete action of the moonlet on the ring particles happens at this scattering plane. The scattering operator relates the azimuthal mass flux entering the scattering region to the azimuthal mass flux leaving the scattering region

$$|J_{\tilde{y}}(\tilde{x}', \tilde{y}' = 0^\pm, \tilde{z}')| = \iint d\tilde{x} d\tilde{z} A(\tilde{x}', \tilde{z}' | \tilde{x}, \tilde{z}) |J_{\tilde{y}}(\tilde{x}, \tilde{z}, \tilde{y} = 0^\mp)|. \quad (9)$$

Mass conservation is expressed as a condition for the scattering operator

$$\iint d\tilde{x}' d\tilde{z}' A(\tilde{x}', \tilde{z}' | \tilde{x}, \tilde{z}) = 1. \quad (10)$$

In this formulation particle accretion by the moonlet is ignored here.

For the numerical calculation of the scattering operator we divide the radial and the vertical direction into bins. The bin  $(j, k)$  describes the region  $(\tilde{x}_j, \tilde{x}_{j+1}) \times (\tilde{z}_k, \tilde{z}_{k+1})$ ,  $j$  being an index in the radial direction and  $k$  one in the vertical direction. In the following, primed bin indices refer to the situation after the scattering by the moonlet and unprimed ones to the situation before.

The discretized scattering operator is then calculated by

$$A(j', k' | j, k) = \frac{N(j', k' | j, k)}{N(j, k)}, \quad (11)$$

where  $N(j, k)$  is the number of test particles starting in bin  $(j, k)$ . We use an averaging procedure to calculate the number of test particles  $N(j', k' | j, k)$  starting in bin  $(j, k)$  and ending in bin  $(j', k')$ . For each radial end bin  $j'$ , describing the interval  $(\tilde{x}_{j'}, \tilde{x}_{j'+1})$ , the time per orbit, the test particle will stay in this radial end bin is calculated (Spahn, 1987)

$$p(j') = \frac{1}{\pi} \left| \arccos\left(\frac{\tilde{a} - \tilde{x}_{j'+1}}{\tilde{e}}\right) - \arccos\left(\frac{\tilde{a} - \tilde{x}_{j'}}{\tilde{e}}\right) \right|. \quad (12)$$

$N(j', k' | j, k)$  is then calculated by

$$N(j', k' | j, k) = \sum_n p^{(n)}(j') \delta^{(n)}(k') \delta^{(n)}(j, k), \quad (13)$$

where the sum is over all test particles.  $\delta(j, k)$  is 1 for test particles starting in bin  $(j, k)$  and is 0 otherwise.  $\delta(k')$ , on the other hand, is 1 for test particles ending in bins with vertical bin index  $k'$  and is 0 otherwise. The superscript  $(n)$  denotes values of these functions for the  $n$ th test particle.

Outside the scattering region we describe the ring using hydrodynamical equations. We assume that the fluid parcels entering and leaving the scattering region have a Keplerian azimuthal mean velocity  $\tilde{u}_{\tilde{y}}(\tilde{x}) = -3\tilde{x}/2$ . The azimuthal mass flux at the scattering plane is then (Spahn and Wiebicke, 1989)

$$J_{\tilde{y}}(\tilde{x}, \tilde{y} = 0^\pm, \tilde{z}) = \rho(\tilde{x}, \tilde{y} = 0^\pm, \tilde{z}) \tilde{u}_{\tilde{y}}(\tilde{x}), \quad (14)$$

where  $\rho$  denotes the mass density. The mass transfer through the scattering region is thus calculated by

$$\rho(j', k') = \frac{1}{|\tilde{u}_{\tilde{y}}(j')|} \sum_{j, k} A(j', k' | j, k) \rho(j, k) |\tilde{u}_{\tilde{y}}(j)|. \quad (15)$$

We assume the ring to be in a quasi-equilibrium state before the encounter with the moonlet. In the following, all quantities of the unperturbed ring have the subscript 0. The surface mass density  $\Sigma_0$  shall be constant, so that the mass density for a thin but multilayered disk is given by

$$\rho_0(\tilde{x}, \tilde{y}, \tilde{z}) = \frac{\Sigma_0/h}{\sqrt{2\pi\tilde{c}_{z0}^2}} \exp\left(-\frac{\tilde{z}^2}{2\tilde{c}_{z0}^2}\right) \quad (16)$$

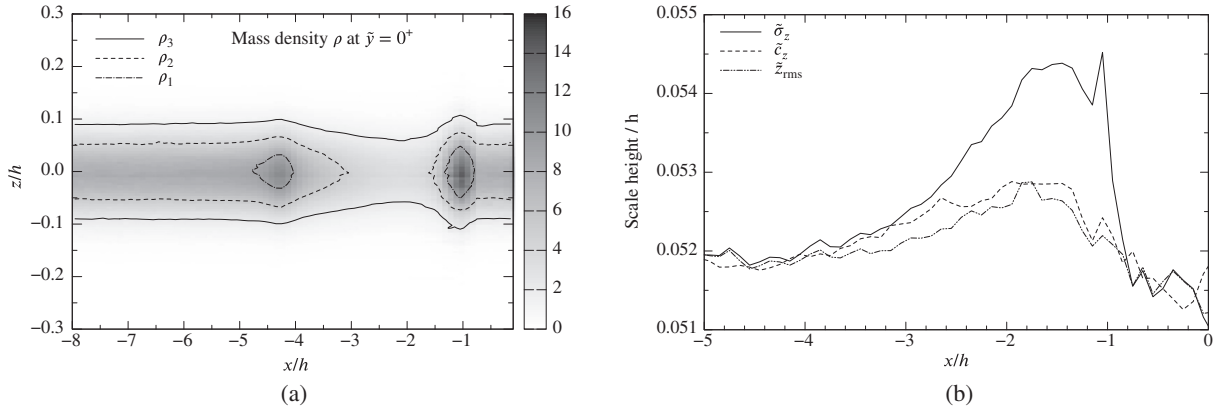


**Fig. 1.** (a) Mass density  $\rho$  scaled by the unperturbed surface mass density over the Hill scale  $\Sigma_0/h$ . This contour plot shows the mass density as a function of the radial coordinate  $x$  and the vertical coordinate  $z$  after scattering by a moonlet with a Hill radius of 300 m. The velocity dispersion of the unperturbed ring is chosen to be  $c_0 = 3.9$  mm/s, corresponding to  $\tilde{c}_z = 0.052$ . The contour lines are for  $\rho_1 = 1.15 \rho_0(\tilde{z} = 0)$ ,  $\rho_2 = \rho_0(\tilde{z} = \tilde{c}_z)$  and  $\rho_3 = \rho_0(\tilde{z} = \sqrt{3}\tilde{c}_z)$ , where  $\rho_0(\tilde{z})$ , given by Eq. (16), is the mass density before the scattering by the moonlet. Clearly seen is the less dense gap region between  $1.5 \leq |\tilde{x}| \leq 4$ . The border of the almost unchanged horseshoe ringlet region is marked by the density peak at  $|\tilde{x}| \approx 1$  (Spahn and Wiebicke, 1989). (b) Ring thickness as function of the radial coordinate  $x$  after the scattering by the same moonlet measured by: standard deviation  $\tilde{\sigma}_z$  of the vertical mass density profile, root mean square  $\tilde{z}_{\text{rms}}$  of the vertical excursions, and vertical thermal velocity  $\tilde{c}_z$ , all at  $\tilde{y} = 0^+$ . All three are within a few percent of the values before the scattering by the moonlet, illustrating that the moonlet's gravity alone (without collisions between ring particles, which will partly transfer lateral induced thermal motion into the vertical direction, see Section 2.3) does not induce considerable vertical excursions of ring particles.

(Simon and Jenkins, 1994; Schmidt et al., 1999).

The two plots in Fig. 1 are made for a moonlet with 300 m Hill radius and the orbital parameters of Earhart (Tiscareno et al., 2010). We have chosen the velocity dispersion of the unperturbed ring to be  $c_0 = 3.9$  mm/s, which is a reasonable value for Saturn's A ring (Sremčević et al., 2008). Using  $c_0^2 = c_{x0}^2 \left\{ 1 + (c_{y0}/c_{x0})^2 + (c_{z0}/c_{x0})^2 \right\}$  and the ratios  $c_{z0}/c_{x0} = 0.65$  and  $c_{y0}/c_{x0} = 0.5$ , this value of  $c_0$  corresponds to the scaled velocity dispersion components  $\tilde{c}_{x0} = 0.08$ ,  $\tilde{c}_{y0} = 0.04$  and  $\tilde{c}_{z0} = 0.052$ . Because of the point symmetry of the Hill Eqs. (3), we show only values for  $\tilde{x} \leq 0$  in the plots.

Fig. 1a shows the mass density  $\rho$  scaled by  $\Sigma_0/h$  after the scattering by the moonlet. The mass density in the regions  $|\tilde{x}| < 1$  and  $|\tilde{x}| > 5$  is nearly unchanged, whereas the gap region  $1.5 < |\tilde{x}| < 4$  has a considerably lower mass density than the ring before the scattering by the moonlet. There are two regions of high mass density around  $|\tilde{x}| = 1$  and  $|\tilde{x}| = 4.25$ . The solid line ( $\phi = 0$ ) in Fig. 3b shows the corresponding surface mass density.

Also shown are three contour lines, corresponding to characteristic values of the unperturbed mass density  $\rho_0$  given by Eq. (16). The first contour line is for  $\rho_1 = 1.15 \cdot \rho_0(\tilde{z} = 0)$ , i.e. 15 percent larger than the maximal value of  $\rho_0$ . The second contour line is for the mass density value  $\rho_2 = \rho_0(\tilde{z} = \tilde{c}_{z0})$ . For low optical depths  $\tilde{c}_z$  is a good estimate of  $\tilde{z}_{\text{rms}}$ , the root mean square value of the vertical excursion of the ring particles. The third contour line shows the mass density  $\rho_3 = \rho_0(\tilde{z} = \sqrt{3}\tilde{c}_{z0})$ , where  $z = \sqrt{3}\tilde{c}_z$  is half of the effective geometric thickness of the ring. The effective geometric thickness  $H_{\text{eff}} = \sqrt{12}\tilde{z}_{\text{rms}} \approx \sqrt{12}\tilde{c}_z$  of the ring corresponds to the total thickness of a uniform vertical mass density profile with the same standard deviation as a Gaussian one.

Fig. 1b shows different measures of the ring thickness after the scattering by the moonlet. To calculate the ring thickness from the mass density, we use an expression of the mass in bin  $(j', k')$  divided by the total mass in bins with bin index  $j'$

$$q(j', k') = \frac{\rho(j', k')}{\sum_{k'} \rho(j', k')}, \quad (17)$$

where we assumed uniform bin sizes. As a quantity,  $q$  describes the distribution of mass in the vertical direction and formally behaves like a probability, i.e.  $0 \leq q(j', k') \leq 1$  and  $\sum_{k'} q(j', k') = 1$ .

The vertical displacement of the ring plane from  $\tilde{z} = 0$ , calculated from the mass density, is then given by

$$\tilde{\mu}_{z,j'} = \sum_{k'} \tilde{z}_{k'} q(j', k'), \quad (18)$$

with  $\tilde{z}_{k'}$  being the midpoint of the vertical interval  $(\tilde{z}_{k'}, \tilde{z}_{k'+1})$ . The vertical displacement should be zero<sup>2</sup> for the unperturbed mass density  $\rho_0$  and the values after the scattering by the moonlet do not differ significantly from zero.

We now express the vertical scale height of the ring by the standard deviation of the vertical mass density profile

$$\tilde{\sigma}_z(j') = \left( \sum_{k'} (\tilde{z}_{k'} - \tilde{\mu}_{z,j'})^2 q(j', k') \right)^{1/2}. \quad (19)$$

As a second measure of ring thickness, we calculated the root mean square value of the vertical excursion of ring particles directly from the results of test particle integrations. With the averaging procedure of Eq. (12),  $\tilde{z}_{\text{rms}}$  is given by

$$\tilde{z}_{\text{rms},j'} = \left( \frac{\sum_n p^{(n)}(j') [\tilde{z}^{(n)} - \langle \tilde{z} \rangle_j]^2}{\sum_n p^{(n)}(j')} \right)^{1/2}, \quad (20)$$

with

$$\langle \tilde{z} \rangle_j = \frac{\sum_n \tilde{z}^{(n)} p^{(n)}(j')}{\sum_n p^{(n)}(j')}. \quad (21)$$

Further, the vertical velocity dispersion  $\tilde{c}_z$  (Section 2.2.3) is a third measure of the ring thickness.

For the unperturbed mass density  $\rho_0$ , both  $\tilde{\sigma}_{z0}$  and  $\tilde{z}_{\text{rms}0}$  equal  $\tilde{c}_{z0}$ . The values after the scattering by the moonlet shown in Fig. 1b are within 6 percent of the values of the unperturbed ring. Calculations for moonlets with different Hill radii from 50 m to 500 m confirm that the difference of the unperturbed values to the ones after the scattering by the moonlet are small, e.g. a few percent. However, this picture changes drastically if a moonlet on an inclined orbit is considered, which is a topic of ongoing work.

<sup>2</sup> If  $\tilde{z}(t')$  is a solution of the Hill Eqs. (3), then  $-\tilde{z}(t')$  is also a solution. For a distribution of initial conditions like Eq. (6), which is invariant under the transformation  $z \rightarrow -z$ , the vertical displacement has to be zero.

Because the moonlet does not induce considerable vertical excursions of ring particles, we will restrict the hydrodynamical description in Section 2.3 to the ring plane (using vertically averaged equations) and model the vertical propeller structure by the granular ring temperature  $T = (\tilde{c}_x^2 + \tilde{c}_y^2 + \tilde{c}_z^2)/3$ .

### 2.2.3. Velocity dispersion

In this subsection we determine values of the moonlet-induced thermal velocities after the scattering by the moonlet, which are later used as initial conditions for the hydrodynamical equations. We calculate the thermal speed components  $\tilde{c}_x$ ,  $\tilde{c}_y$  and  $\tilde{c}_z$  by taking the weighted sample standard deviation of  $\tilde{v}_x$ ,  $\tilde{v}_y - 3\tilde{x}/2$  and  $\tilde{v}_z$  for the set of integrated test particles. For  $\tilde{c}_x$ , for example,

$$\tilde{c}_x(j') = \left( \frac{\sum_n p^{(n)}(j') [\tilde{v}_x^{(n)} - \langle \tilde{v}_x \rangle(j')]^2}{\sum_n p^{(n)}(j')} \right)^{1/2}, \quad (22)$$

where  $j'$  denotes the post-encounter radial bin number.

Due to the averaging process (12) our model does not describe moonlet wakes, which are moonlet-induced coherent motions of ring particles (Showalter et al., 1986; Spahn et al., 1994). In our averaged description of the wake region, we might overestimate  $\tilde{c}_x$  and  $\tilde{c}_y$  with Eq. (22), because the averaging process destroys the coherent phase relations and systematic motion looks partly like thermal motion.

Nevertheless our model describes the gap region, in which the maximal propeller heights are reached, quite well. Test particles ending in this region are often on trajectories which are very sensitive to initial conditions (Hénon and Petit, 1986), and their phases are mixed up. Furthermore, wake structures start to dissolve when nearby streamlines cross. For the gap region this happens very fast, i.e. for the middle of the gap at  $|\tilde{x}| = 2.5$  after 0.4 orbits.

Fig. 1b shows  $\tilde{c}_z$  and  $\tilde{z}_{\text{rms}}$ , which do not deviate much at  $\tilde{y} = 0^+$ . In Fig. 2a we compare the mean thermal velocities after the scattering by the moonlet of Fig. 1. The maximal excitation in each case lies near the inner edge of the moonlet-induced gap at a radial position of about  $|\tilde{x}| = 7/4$ .

Fig. 2a also shows that the moonlet induces much more thermal motion in the ring plane than in the vertical direction. Values of the vertical component of the thermal velocity after the scattering by the moonlet are within a few percent of the values before the scattering (see Fig. 1b, where  $\tilde{c}_z$  is plotted on a different scale),

resulting in a ratio  $c_z/c_x$  after the scattering, which is several times smaller than the equilibrium value  $(c_z/c_x)_{\text{eq}} = 0.65$ . The ratio of the horizontal components  $c_y/c_x$ , however, is close to the equilibrium value  $(c_y/c_x)_{\text{eq}} = 0.5$ , as expected if the particle orbits after the scattering are well described by Eq. (4). Therefore, although the gravitational interaction with the moonlet induces some thermal motion in vertical direction, it is negligible compared to the thermal motion induced in the ring plane for moonlets on non-inclined orbits.

The considerable thermal motion induced in lateral direction will be shown to be the reason for the attained propeller heights in Section 3. Collisions among ring particles transfer the thermal motion into the vertical direction until the quasi-equilibrium ratio  $(c_z/c_x)_{\text{eq}}$  is established, which will happen on collisional time scales after a few collisions per particle (cf. Section 4.1).

Fig. 2b shows the  $x$ -component of the velocity dispersion, scaled by  $\Omega_0 h$ , at  $\tilde{y} = 0^+$  after the scattering by moonlets with Hill radii of 50–500 m. For the larger moonlets, with a Hill radius above 100 m, the  $x$ -component of the velocity dispersion in the gap region, especially the maximal value of  $\tilde{c}_x$ , scales well with the Hill radius of the moonlets.

### 2.3. Hydrodynamic flow

Outside of the scattering region we describe the ring with hydrodynamical equations (Seiß and Spahn, 2011; Schmidt et al., 2001; Spahn et al., 1997). We model the thickness of the ring through the granular ring temperature, and use vertically averaged balance equations. The mass and momentum balance are given by

$$\frac{\partial \Sigma}{\partial t} + \nabla \cdot (\Sigma \mathbf{u}) = 0 \quad (23)$$

$$\frac{\partial \mathbf{u}}{\partial t} + (\mathbf{u} \cdot \nabla) \mathbf{u} = \mathbf{f} - \frac{1}{\Sigma} \nabla \cdot \mathbf{P}. \quad (24)$$

Here  $\Sigma$ ,  $\mathbf{u}$ ,  $\mathbf{f}$  and  $\mathbf{P}$  are the surface mass density, the mean velocity, external volume forces, and the pressure tensor. The pressure tensor is given in Newtonian form

$$\mathbf{P} = p\mathbf{I} - 2\Sigma\nu\mathbf{D} - \Sigma\zeta(\nabla \cdot \mathbf{u})\mathbf{I}, \quad (25)$$

where  $\mathbf{I}$  is the unit tensor. The vertically integrated pressure, kinematic bulk and shear viscosity are denoted by  $p$ ,  $\zeta$  and  $\nu$ . The traceless shear tensor  $\mathbf{D}$  is given by

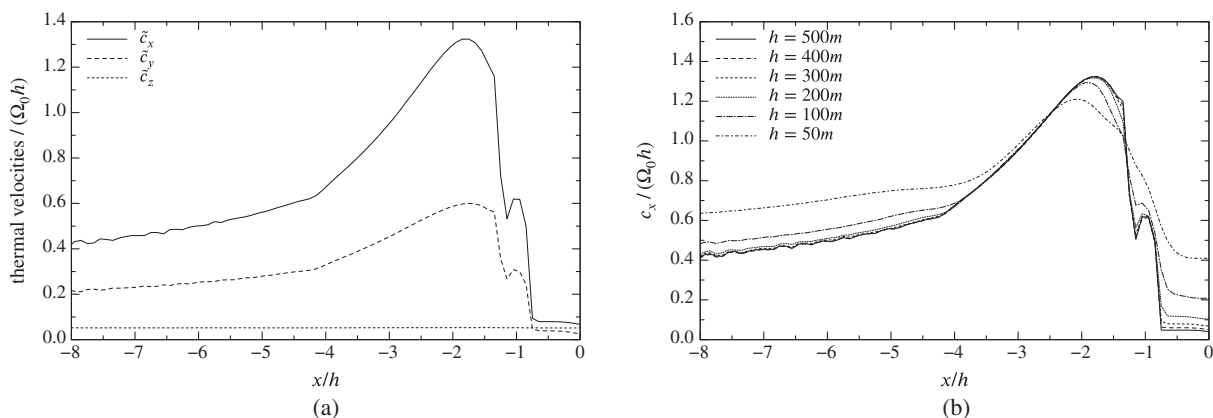


**Fig. 2.** Moonlet-induced thermal velocities as functions of the radial coordinate  $\tilde{x}$  at  $\tilde{y} = 0^+$ . All thermal velocities are scaled by  $\Omega_0 h$ . (a) Thermal velocities after the gravitational scattering by a moonlet with 300 m Hill radius. The moonlet induces much more thermal motion in the ring plane than in vertical direction. For comparison, the values of the thermal velocities before the encounter with the moonlet are  $\tilde{c}_{x0} = 0.08$ ,  $\tilde{c}_{y0} = 0.04$  and  $\tilde{c}_{z0} = 0.052$ , corresponding to  $c_0 = 3.9$  mm/s. After the scattering by the moonlet, these values are obtained in the radial region  $|\tilde{x}| < 0.75h$ , because the ring particles are on horseshoe orbits and their minimal distance to the moonlet remains large, so that there is no considerable induced thermal motion. The  $\tilde{c}_z$  curve is also plotted in Fig. 1b on a different scale. (b) Comparison of the radial thermal velocity  $\tilde{c}_x$  after the scattering by moonlets with different Hill radii. In the gap region  $-4 \leq \tilde{x} \leq -1.5$  the radial thermal velocity scales well with  $\Omega_0 h$  for the larger moonlets ( $h = 100$  m and above).

$$\mathbf{D} = \frac{1}{2}(\nabla \circ \mathbf{u} + \mathbf{u} \circ \nabla) - \frac{1}{3}(\nabla \cdot \mathbf{u})\mathbf{I}, \quad (26)$$

where  $(\nabla \circ \mathbf{u})_{jk} = \nabla_j u_k$  and  $(\mathbf{u} \circ \nabla)_{jk} = \nabla_k u_j$ .

With these closures the energy balance of the ring particle's random motion reads

$$\frac{3}{2}\Sigma \left( \frac{\partial T}{\partial t} + (\mathbf{u} \cdot \nabla)T \right) = -\mathbf{P} : \boldsymbol{\epsilon} - \nabla \cdot \mathbf{Q} - \Gamma, \quad (27)$$

where  $T = (c_x^2 + c_y^2 + c_z^2)/3$  is the granular ring temperature and  $\mathbf{Q} = -\kappa_D \nabla T$  the heat flow in the ring with heat conductivity  $\kappa_D$ . The friction term  $\mathbf{P} : \boldsymbol{\epsilon}$  with the shear tensor  $\boldsymbol{\epsilon} = (\nabla \circ \mathbf{u} + \mathbf{u} \circ \nabla)/2$  describes the viscous heating of the ring, and  $\Gamma$  accounts for the energy loss due to inelastic collisions.

### 2.3.1. Mass and momentum balance

The gravitational scattering by the moonlet opens a gap. The diffusion of the ring particles, described by the nonlinear viscous diffusion equation

$$\frac{\partial \Sigma}{\partial t} + (\Omega(r) - \Omega_0) \frac{\partial \Sigma}{\partial \varphi} - \frac{3}{r} \frac{\partial}{\partial r} \left[ \sqrt{r} \frac{\partial}{\partial r} (\sqrt{r} v \Sigma) \right] = 0 \quad (28)$$

for the surface mass density  $\Sigma$ , tends to smooth out the induced structures (Spahn and Sremčević, 2000; Sremčević et al., 2002). Here, the radial coordinate  $r$  describes the distance to Saturn's center and  $\varphi$  denotes the azimuthal coordinate in the corotating frame.

In order to solve Eq. (28) we apply the following simplifications, already used by Sremčević et al. (2002): Let  $\sigma_1 = \Sigma - \Sigma_0$ , where  $\Sigma_0$  is the equilibrium value of the surface mass density of the unperturbed ring. We assume the propeller to be a stationary structure ( $\partial \sigma_1 / \partial t = 0$ ) in the co-moving frame. In the special case of constant kinematic viscosity  $\nu_0$  and without curvature terms, which is consistent with the Hill approximation of the gravitational scattering, Eq. (28) reduces to a linear partial differential equation

$$K \bar{x} \frac{\partial \sigma_1}{\partial \varphi} = - \frac{\partial^2 \sigma_1}{\partial \bar{x}^2}, \quad (29)$$

where the constant  $K$  is given by

$$K = \frac{\Omega_0 a_0^2}{2\nu_0} \left( \frac{h}{a_0} \right)^3 \quad (30)$$

and defines by  $a_0 K$  a characteristic azimuthal length scale of the viscous diffusion. The diffusion timescale is  $t_{\text{diff}} = h^2 / \nu_0$ , where we use the Hill radius  $h$  as characteristic radial length scale. During that time, ring particles with radial distance  $h$  to the moonlet, move the azimuthal length  $y_{\text{diff}} = 3a_0 K$  away from the moonlet.

Eq. (29) is point symmetric with respect to the position of the moonlet ( $\bar{x} = \bar{y} = \bar{z} = 0$ ). For the region defined by  $\bar{x} < 0$  and  $\varphi > 0$ , with boundary conditions

$$\sigma_1(\bar{x} < 0, \varphi = 0^+) = \sigma_{1,\text{ini}} \quad (31)$$

$$\sigma_1(\bar{x} \rightarrow -\infty, \varphi) = 0 \quad (32)$$

$$\sigma_1(\bar{x}, \varphi \rightarrow \infty) = 0, \quad (33)$$

Sremčević et al. (2002) derived several Green's functions for different constraints at  $\bar{x} = 0, \varphi > 0$ . The Green's function that matched their numerical solution best is an equally weighted superposition of Green's functions for the two cases

$$\sigma_1(\bar{x} = 0, \varphi) = 0 \quad (34)$$

$$\frac{\partial \sigma_1}{\partial \bar{x}}(\bar{x} = 0, \varphi) = 0. \quad (35)$$

We use this Green's function, given by

$$G(\bar{x}, \varphi) = \frac{\sqrt{3}}{2} (-\bar{x}_0) (3\varphi)^{2/3} \exp\left(\frac{\bar{x}_0^3 + \bar{x}^3}{9\varphi}\right) \text{Bi}\left((3\varphi)^{2/3} \bar{x}_0 \bar{x}\right), \quad (36)$$

with the scaled azimuth  $\phi = \varphi/K$ , and the Airy function  $\text{Bi}(z)$ , to calculate the surface mass density via

$$\sigma_1(\bar{x}, \phi) = \int_{-\infty}^0 d\bar{x}_0 \sigma_{1,\text{ini}}(\bar{x}_0) G(\bar{x}, \phi; \bar{x}_0). \quad (37)$$

As initial surface mass density  $\sigma_{1,\text{ini}}$  we use the vertically integrated mass density calculated with the scattering operator (15), shown in Fig. 3b as solid line, and numerically integrate Eq. (37). The two plots in Fig. 3 are again made for a moonlet with 300 m Hill radius and the orbital parameters of Earhart.

We used the value  $\nu_0 = 0.011 \text{ m}^2/\text{s}$  for the kinematic viscosity, which is reasonable for the central part of Saturn's A ring (Tiscareno et al., 2007). Here, we used this value for the ring in the vicinity of Earhart, because measured viscosity values between the Encke and Keeler gaps are still sparse (Colwell et al., 2009; Tiscareno et al., 2007), and this value is consistent with the chosen velocity dispersion  $c_0 = 3.9 \text{ mm/s}$  (using Eq. (44)).

Fig. 3a shows the surface mass density after the scattering by the moonlet as function of  $x$  and  $\phi = y/(a_0 K)$ . White contour lines represent surface mass density values below  $\Sigma_0$ , showing the evolution of the gap. Black contour lines enclose regions of enhanced surface mass density compared to  $\Sigma_0$ . To illustrate the gap-closing, we plotted the surface mass density as a function of the radial coordinate  $x$  for different longitudes  $\phi$ , shown in Fig. 3b.

The azimuthal extent of the moonlet-induced partial gap scales with  $a_0 K$ . The value of the scaling constant  $K$  for a moonlet with 300 m Hill radius, Earhart's semimajor axis and with a kinematic viscosity of  $\nu_0 = 0.011 \text{ m}^2/\text{s}$  is

$$K = 1.15 \times 10^{-3} \left( \frac{h}{300 \text{ m}} \right)^3 \left( \frac{0.011 \text{ m}^2/\text{s}}{\nu_0} \right) \left( \frac{133797.84 \text{ km}}{a_0} \right)^{5/2}, \quad (38)$$

resulting in  $a_0 K = 515h$ , and thus,  $\phi = y/(a_0 K) = 1$  corresponds to  $y = 515h$ .

Because  $K \propto h^3$ , the importance of the mass diffusion process, in the first few orbits<sup>3</sup> after the scattering by the moonlet, depends strongly on the Hill radius of the moonlet. For large moonlets, e.g.  $h = 500 \text{ m}$ , the value of the surface mass density remains similar to the value at  $\phi = 0$  much longer downstream than for small moonlets.

### 2.3.2. Energy balance

In this subsection we will consider the relaxation of the moonlet-induced thermal heating by dissipative particle interaction, expanding on the approach used in Hoffmann et al. (2013). Although the vertically ineffective gravitational interaction of ring particles with the moonlet cannot explain the vertical height of propeller structures, the moonlet induces a considerable amount of thermal (random) motion in the lateral direction.

Due to mutual collisions between ring particles, the thermal motion induced in the lateral direction will be converted to vertical thermal motion till the ratio  $c_z/c_x$  reaches its local equilibrium value. This asymptotic value of  $c_z/c_x$  is established very quickly, after a few collisions per particle (Hämeen-Anttila and Lukkari, 1980; Hämeen-Anttila and Salo, 1993), which is also demonstrated with N-body box simulations later. Therefore, we use the granular temperature  $T$  to model the evolution of the vertical propeller structure, inferring the thickness of the ring from  $T$  and the equilibrium value of  $c_z/c_x$ .

<sup>3</sup> Ring particles move  $|y_{\text{orbit}}| = 3\pi|x|$  per orbit downstream away from the moonlet, where  $x$  denotes the radial distance to the moonlet. For particles at  $|x| = 2h$  and the ring parameters used in Fig. 3, the characteristic azimuthal length scale of the viscous diffusion is  $a_0 K = 27|y_{\text{orbit}}|$ .

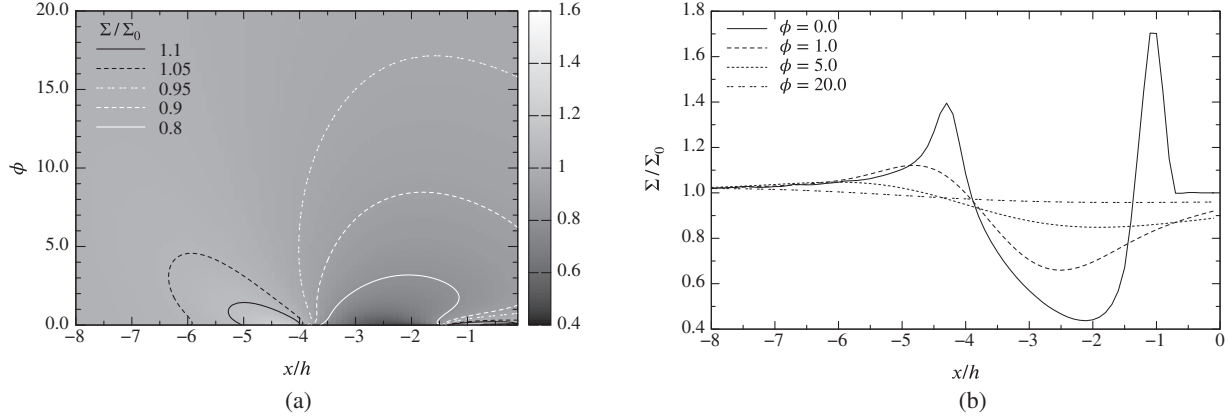


**Fig. 3.** (a) Contour plot of the surface mass density downstream of a moonlet with 300 m Hill radius and the orbital parameters of Earhart. The contour plot shows the mass density as a function of the radial coordinate  $x$  and the scaled azimuthal coordinate  $\phi = y/(a_0K)$  (see Eq. (30)). White contour lines represent surface mass density values below  $\Sigma_0$ , showing the evolution of the gap. Black contour lines enclose regions of enhanced surface mass density compared to  $\Sigma_0$ . (b) Surface mass density as a function of the radial coordinate  $x$  for different scaled longitudes  $\phi$ , illustrating the gap-closing. The solid line shows the surface mass density after the scattering by the moonlet.

The thermal energy balance equation in the corotating frame reads

$$\frac{3}{2}\Sigma\left\{\frac{\partial T}{\partial t} + (\Omega - \Omega_0)\frac{\partial T}{\partial\phi} + u_r\frac{\partial T}{\partial r}\right\} = -\mathbf{P}:\boldsymbol{\epsilon} - \nabla\cdot\mathbf{Q} - \Gamma. \quad (39)$$

Regarding the relaxation of the induced thermal motion, there are three relevant timescales involved: (i) the local equilibrium value of  $c_z/c_x$  is reached on collisional timescales  $t_{\text{coll}} = \omega_c^{-1}$ , where  $\omega_c$  is the collision frequency. According to  $\omega_c = 3\Omega\tau$ , where  $\tau$  is the dynamical optical depth

$$\tau = \int_0^\infty \pi R^2 n(R) dR, \quad (40)$$

with the particle radius  $R$  and particle size distribution  $n(R)$ , there are about 10 collisions per particle per orbit in Saturn's A ring where we used  $\tau = 0.5$ . The resulting timescale is thus smaller than an orbital period. (ii) The exponential decay of the granular temperature takes a few orbits, in the case of a moonlet with 300 m Hill radius about 20 orbits. (iii) Stochastic diffusion processes, like the gap-closing or heat conduction, operate on the mass diffusion timescale  $t_{\text{diff}} = (\Delta r)^2/v$ . For a moonlet with 300 m Hill radius, for example, the gap-closing takes hundreds of orbits (Sremčević et al., 2002).

Especially for large moonlets we expect these three timescales to separate clearly, and thus, to decouple. In the following, we neglect heat conduction and consider, for simplicity, only viscous heating and the energy loss due to inelastic collisions (granular cooling), because we are mainly interested in the exponential decay of the granular temperature and heat conduction operates on the slower diffusive timescale  $t_{\text{diff}}$ .

Furthermore, we assume the propeller to be a stationary structure in the co-moving frame ( $\partial T/\partial t = 0$ ), thus obtaining

$$\frac{3}{2}(\Omega - \Omega_0)\frac{\partial T}{\partial\phi} = \frac{9}{4}v\Omega_0^2 - k_3\Omega_0\tau(1 - \varepsilon^2)T, \quad (41)$$

where we used  $\mathbf{P}:\boldsymbol{\epsilon} = -9v\Omega_0^2\Sigma/4$  for the friction term, regarding just the dominant Kepler shear. For the cooling term we used  $\Gamma = k_3\Omega_0\tau(1 - \varepsilon^2)\Sigma T$  with a constant coefficient of restitution  $\varepsilon = 0.4$  and with  $k_3 = 1.5$ , corresponding to an energy loss rate

$$\dot{E}_{\text{coll}} = -\frac{\omega_c}{6}(1 - \varepsilon^2)\Sigma c^2 \quad (42)$$

(Morishima and Salo, 2006), with collision frequency  $\omega_c = 3\Omega\tau$  (Schmidt et al., 2009), and granular temperature  $c^2 = 3T$ .

We apply a kinematic viscosity of the form  $v = v_* + v_l$ , where,  $v_*$  is assumed to be independent of the granular ring temperature, whereas the local viscosity  $v_l$  given by

$$v_l(\tau, T) = \beta(\tau)3T = \frac{k_1\tau}{\Omega_0(1 + \tau^2)}3T \quad (43)$$

(with  $k_1 = 0.15$ , Goldreich and Tremaine, 1978) depends on the ring temperature. With this viscosity and the constant coefficient of restitution, viscous heating and collisional cooling balance at a local equilibrium temperature

$$T_{\text{eq}}(\tau) = \frac{9v_*(\tau)\Omega_0}{4k_3(1 - \varepsilon^2)\tau - 27\beta(\tau)\Omega_0}, \quad (44)$$

which depends on the local optical depth, or assuming equally sized ring particles with particle radius  $R_p$  and mass  $m_p$ , via  $\tau = \pi R_p^2\Sigma/m_p$ , on the surface mass density  $\Sigma$ . The temperature of the unperturbed ring before the encounter with the moonlet is denoted by  $T_0 = T_{\text{eq}}(\tau_0)$ .

With these assumptions Eq. (41) becomes a linear ordinary differential equation in  $\tilde{y}$ . Because of the neglected curvature, Eq. (41) becomes also point symmetric to the origin of the coordinate frame. In the following we describe the case  $\tilde{y} > 0$  and  $\tilde{x} < 0$  which is, because of the point symmetry, no restriction. With  $(\Omega(r) - \Omega_0)\partial/\partial\phi = -3/2\Omega_0\tilde{x}\partial/\partial\tilde{y}$ , Eq. (41) then reads

$$|\tilde{x}|\frac{\partial T}{\partial\tilde{y}} = v_*(\tau)\Omega_0 - \left(\frac{4}{9}k_3\tau(1 - \varepsilon^2) - 3\beta(\tau)\Omega_0\right)T. \quad (45)$$

The solution of this equation can be written in the form

$$T(|\tilde{x}|, \tilde{y}) = T_{\text{ini}}(|\tilde{x}|)e^{-\gamma(|\tilde{x}|, \tilde{y})} + e^{-\gamma(|\tilde{x}|, \tilde{y})} \int_0^{\tilde{y}} f(|\tilde{x}|, \tilde{y}')e^{\gamma(|\tilde{x}|, \tilde{y}')} d\tilde{y}', \quad (46)$$

with the functions

$$\gamma(|\tilde{x}|, \tilde{y}) = \frac{1}{|\tilde{x}|} \int_0^{\tilde{y}} \left(\frac{4}{9}k_3\tau(1 - \varepsilon^2) - 3\beta(\tau)\Omega_0\right) d\tilde{y}' \quad (47)$$

$$f(|\tilde{x}|, \tilde{y}) = \frac{v_*(\tau)\Omega_0}{|\tilde{x}|}.$$

The plots in Fig. 4 show the downstream temperature relaxation. Again they are made for a moonlet with 300 m Hill radius and the orbital parameters of Earhart. For simplicity, we assume  $v_*$  to be constant on timescales relevant to the exponential decay of the temperature. In order to match the chosen velocity dispersion  $c_0 = 3.9$  mm/s we calculated  $v_* = 0.004$  m<sup>2</sup>/s using Eq. (44).

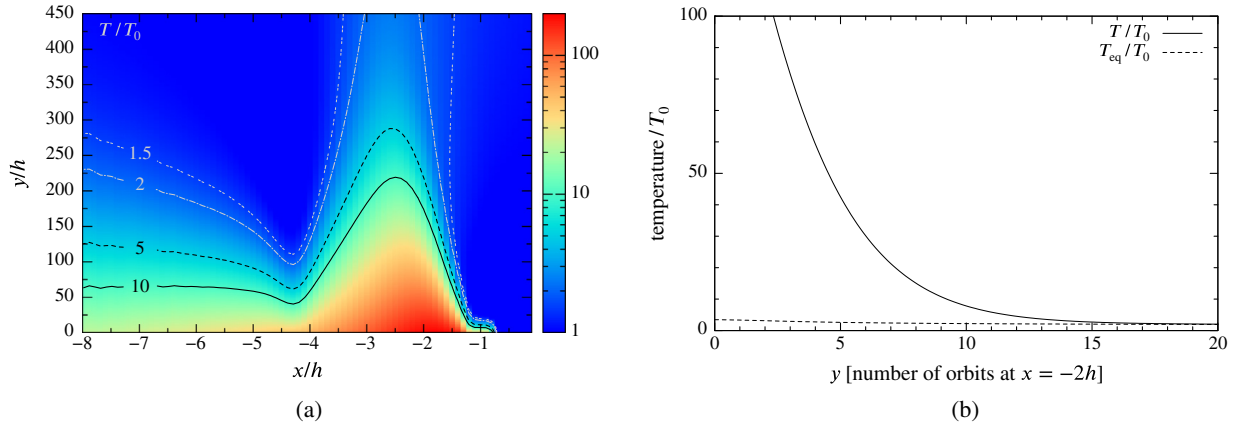


**Fig. 4.** Downstream temperature relaxation for a moonlet with a 300 m Hill radius. (a) Contour plot of the temperature decrease downstream of the moonlet. The contour plot shows the granular ring temperature  $T$ , scaled by the granular temperature of the unperturbed ring  $T_0$ , as function of the radial coordinate  $x$  and the azimuthal length  $y$ . To better compare with Fig. 3:  $y = 450h$  corresponds to  $\phi = y/(a_0K) = 0.87$ . (b) Temperature relaxation at radial position  $x = -2h$ . The solid line shows the temperature relaxation of the ring, the dashed line corresponds to the equilibrium temperature  $T_{eq}$ , for which viscous heating and collisional cooling are in balance. For about 20 orbits (corresponding to  $\phi = 0.73$  in Fig. 3), the ring temperature decreases exponentially to the local equilibrium temperature. Afterwards, the viscous heating and the collisional cooling are balanced and the ring temperature evolves as a function of the surface mass density of the ring.

This results in a total quasi-equilibrium kinematic viscosity of  $\nu = 0.011 \text{ m}^2/\text{s}$  of the unperturbed ring (reasonable for the central part of Saturn’s A ring, Tiscareno (2007)), which we use here for the ring in the vicinity of Earhart. Important for the exponential temperature decay is the value of  $\nu_i$ , the temperature dependent part of the viscosity.

Fig. 4a shows a contour plot of the ring temperature  $T$  scaled by the unperturbed ring temperature  $T_0$ , illustrating the azimuthal temperature decay for different radial regions. Ring particles with  $|x| < 0.75h$  are on horseshoe orbits and their minimal distance to the moonlet is large, so that there is no considerable thermal excitation. The gap region, on the other hand, is highly excited for quite an azimuthally extended range. Fig. 4b shows the azimuthal temperature evolution downstream of the moonlet, at fixed radial position  $x = -2h$ . Also, the local equilibrium temperature  $T_{eq}$  is shown as function of the surface mass density. For about 20 orbits,<sup>4</sup> the ring temperature decreases exponentially to the local equilibrium temperature. Afterwards, the viscous heating and the collisional cooling are balanced and the ring temperature evolves as a function of the surface mass density of the ring. In this case the temperature gets within a margin of 10% of  $T_{eq}$  in about 18 orbits.

The influence of the mass diffusion on the temperature decay depends on the Hill radius of the moonlet. For large moonlets, close in size to ring-moons able to open a circumferential gap, the thermal excitation vanishes much faster than the propeller gap, and thus, the perturbed optical depth stays nearly constant during this cooling process. In this case the solution (46) can be simplified to

$$T_{\text{approx}}(\tilde{x}, \tilde{y}) = (T_{\text{ini}} - T_{\text{eq}}(\tau)) e^{-\lambda(\tilde{x})\tilde{y}} + T_{\text{eq}}(\tau). \quad (48)$$

with  $\gamma(\tilde{x}, \tilde{y}) = \lambda(\tilde{x})\tilde{y}$ . The decay constant  $\lambda$  can then be written in the form

$$\lambda(\tilde{x}) = \frac{2\omega_c(1 - \varepsilon^2)}{9\Omega|\tilde{x}|} - \frac{3\beta\Omega}{|\tilde{x}|}. \quad (49)$$

Fig. 5 illustrates the decoupling of the timescales for the stochastic mass diffusion and the exponential decay of the granular ring temperature. Shown are values calculated from Eq. (49) with optical depths  $\tau_{\text{ini}}$  taken directly after the scattering by the moonlet (open squares) and values taken from fits of Eq. (48) to temperature

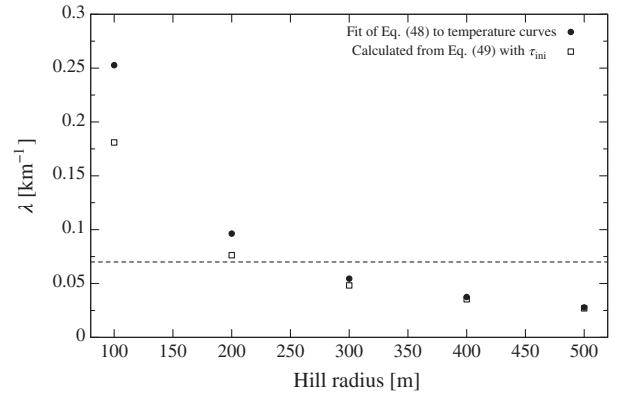


**Fig. 5.** Exponential decay constant  $\lambda$  at  $x = -2h$  for moonlets with different Hill radii. Values denoted by open squares are calculated from Eq. (49) with optical depth  $\tau_{\text{ini}}$  directly after the scattering by the moonlet. Values denoted by filled circles are taken from fits of Eq. (48) to temperature curves calculated from Eq. (46). This plot illustrates how the timescales for the stochastic diffusion causing the gap closing and the exponential decay of the temperature decouple for large moonlets. As orientation the dashed line marks the value of  $0.07 \text{ km}^{-1}$ , measured for the propeller Earhart (Hoffmann et al., 2013).

curves calculated from Eq. (46). As orientation the dashed line marks the value of  $0.07 \text{ km}^{-1}$ , measured for the propeller Earhart (Hoffmann et al., 2013).

### 3. The vertical height of propellers

For a thin but multilayered disk and with the assumption that  $c_z$  is independent of  $z$ , the vertical profile of the mass density can be described well by a Gaussian with standard deviation  $c_z/\Omega_0$  (Stewart et al., 1984; Simon and Jenkins, 1994; Schmidt et al., 1999). We use the effective geometric thickness  $H_{\text{eff}}$  as a measure of the ring thickness and determine the height  $H$  of the propeller structure as half the effective geometric thickness of the ring

$$H = \sqrt{3} \frac{c_z}{\Omega_0}. \quad (50)$$

To determine  $c_z$  as a function of the temperature  $T$ , we use the local equilibrium values of the ratios  $c_z/c_x$  and  $c_y/c_x$ . The collision frequency in the propeller gap region of Earhart, where we expect

<sup>4</sup> Ring particles move  $|y_{\text{orbit}}| = 3\pi|x|$  per orbit downstream away from the moonlet,  $x$  denoting the radial distance to the moonlet. For particles at  $|x| = 2h$  and the ring parameters used in Fig. 4, 20 orbits corresponds to  $\phi = 20|y_{\text{orbit}}|/(a_0K) = 0.73$  in Fig. 3.

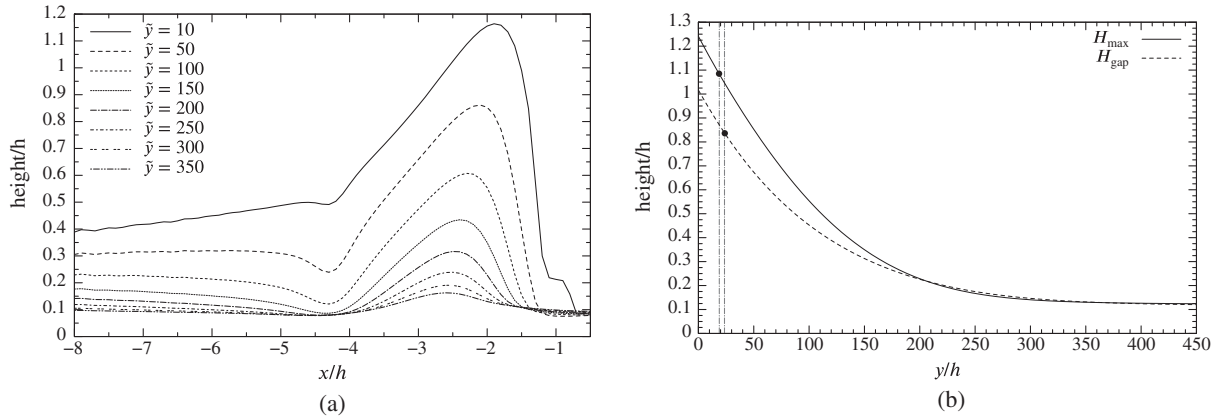


**Fig. 6.** Azimuthal relaxation of the propeller height for a moonlet with 300 m Hill radius. (a) Propeller heights as function of radial coordinate  $\tilde{x}$  for different longitudes. (b) Downstream relaxation of the propeller height. The solid line shows the relaxation at  $\tilde{x} = -2$ , whereas the dashed line shows the propeller height radially averaged over the gap region. We assume that the equilibrium values of  $c_z/c_x$  and  $c_y/c_x$  after the scattering by the moonlet are established after one orbit (see discussion in text), so that the granular temperature describes the propeller height well. After one orbit at radial position  $x = -2h$ , marked by the first dashed vertical line at  $\tilde{y} = 18.9$ , the height is about 1.08 Hill radii or 330 m. Choosing the approximate middle of the gap at  $x = -2.5h$  as a reference (in that case one orbit corresponds to  $y = 23.6h$ , marked by the second dashed line), the averaged propeller height is about 0.84 Hill radii or 250 m. Propeller heights for moonlets with Hill radii from 50 m to 500 m are listed in Table 1.

the largest excitations, is estimated to be about  $\omega_c/\Omega = 1.0$ , corresponding to about 6 collisions per particle per orbit (cf. Hoffmann et al., 2013). This leads, with  $\omega_c = 3\Omega\tau$  (Schmidt et al., 2009), to an optical depth of  $\tau = 0.3$  in the density-depleted gap region of the propeller, which seems reasonable compared to  $\tau = 0.5$  of Saturn's unperturbed A ring. Therefore, we assume in the following, that the equilibrium values of  $c_z/c_x$  and  $c_y/c_x$  are established after one orbit (corresponding to about 6 collisions).

With the relaxed ratios  $(c_z/c_x)_{\text{eq}} = 0.65$  and  $(c_y/c_x)_{\text{eq}} = 0.5$ , we regard  $T = (c_x^2 + c_y^2 + c_z^2)/3$  as a function of only one of the components  $c_x, c_y, c_z$ , for example

$$3T = c_x^2 \left\{ 1 + (c_y/c_x)_{\text{eq}}^2 + (c_z/c_x)_{\text{eq}}^2 \right\}. \quad (51)$$

Using  $c_z = (c_z/c_x)_{\text{eq}} \cdot c_x$ , the z component of the velocity dispersion in terms of  $T$  is given by

$$c_z(T) = \left( \frac{c_z}{c_x} \right)_{\text{eq}} \sqrt{\frac{3T}{1 + (c_y/c_x)_{\text{eq}}^2 + (c_z/c_x)_{\text{eq}}^2}}. \quad (52)$$

The two plots in Fig. 6 are made using the same parameters as were taken for Fig. 4, i.e. a moonlet with 300 m Hill radius, the orbital parameters of Earhart and a velocity dispersion  $c_0 = 3.9$  mm/s of the unperturbed ring. In Fig. 6a, the height of the propeller structure as a function of the radial coordinate  $\tilde{x}$  is plotted for different values of  $\tilde{y}$ . The largest heights are reached in the region between  $\tilde{x} = -4$  and  $\tilde{x} = -1$ , the maximum being at about  $\tilde{x} = -2$  for  $\tilde{y} = 10$  and slowly moving to the radial gap minimum at  $\tilde{x} = -2.5$  (for  $\tilde{y} = 350$ ).

The azimuthal relaxation of the height of the propeller structure, for  $\tilde{x} = -2$ , is shown in Fig. 6b. After one orbit at radial position  $\tilde{x} = -2$ , corresponding to  $\tilde{y} = 18.9$ , the height is about 1.08 Hill radii or 330 m. Furthermore, Fig. 6b sketches the propeller height radially averaged over the gap region. We choose the approximate middle of the gap at  $\tilde{x} = -2.5$  as a reference, and in that case one orbit corresponds to  $\tilde{y} = 23.6$ . At that position the gap-averaged propeller height is 0.84 Hill radii or about 250 m.

Table 1 shows propeller heights for moonlets with different Hill radii.  $H_{\text{max}}$  is the height taken one orbit downstream of the moonlet at radial position  $\tilde{x} = -2$ .  $H_{\text{gap}}$  is the height averaged over the gap region taken one orbit downstream of the moonlet at the approximate middle of the gap. The maximal heights are close to one Hill

**Table 1**

Heights for moonlets with different Hill radii from 50 m to 500 m.  $H_{\text{max}}$  is the height at  $\tilde{x} = -2.0$  and  $\tilde{y} = 18.9$ , corresponding to one orbit downstream of the moonlet.  $H_{\text{gap}}$  is the height averaged over the gap region at azimuthal position  $\tilde{y} = 23.6$  (one orbit downstream of the moonlet at radial position  $\tilde{x} = -2.5$ ). Fig. 6 shows the downstream relaxation of  $H_{\text{max}}$  and  $H_{\text{gap}}$  for a moonlet with 300 m Hill radius.

$h$ (m)	50	100	200	300	400	500
$H_{\text{max}}$ (h)	0.99	1.03	1.07	1.08	1.09	1.10
$H_{\text{gap}}$ (h)	0.86	0.81	0.83	0.84	0.84	0.85

radius for the tested moonlet sizes. The values of the gap averaged height for the moonlets are between 0.81 and 0.86 Hill radii.

For large moonlets, where the optical depth  $\tau$  within the gap stays nearly constant on the timescale of the exponential decay, the approximate solution Eq. (48) can be rewritten to lead to a propeller height of the form

$$H(\tilde{y}) = \sqrt{(H_{\text{max}}^2 + H_0^2) \exp(-\lambda\tilde{y}) + H_0^2}, \quad (53)$$

where  $H_{\text{max}} \propto \sqrt{T_{\text{ini}}}$  and  $H_0 \propto \sqrt{T_{\text{eq}}}$ . This is a suitable equation to be fitted to propeller shadows seen in images taken by the Cassini spacecraft (Hoffmann et al., 2013).

#### 4. Comparison to N-body simulations

In order to verify the assumptions made in the derivation of the extended propeller model and to compare results, we performed N-body box simulations of propeller moonlets embedded in planetary rings.

The method of N-body box simulations, in which a co-moving ring patch with periodic boundary conditions is simulated, was introduced by Wisdom and Tremaine (1988) and subsequently further developed (e.g. Salo, 1991, 1995). In our simulations we use the version by Salo et al. (2001). This code, which was also applied in the propeller simulations of Seiß et al. (2005) and Sremčević et al. (2007), has an option to include a perturbing moonlet in the center of the calculation region and to replace the periodic azimuthal boundaries with a constant inflow of fresh particles.

The simulations were performed under simplifying assumptions like a constant coefficient of restitution (except for X12 and X13 where the Bridges et al. (1984) dependence on the impact velocity is used) and mono-sized, non-gravitating ring particles

**Table 2**

Parameters of N-body box simulations with an embedded moonlet.  $R_{\text{moon}}$  denotes the radius of the moonlet,  $h$  its Hill radius and  $\rho_{\text{moon}}$  its mass density. The results of the simulations can be scaled to other planetocentric distances  $a_{\text{moon}}$ , provided the ratio  $h/R_m \propto a_{\text{moon}} \rho_{\text{moon}}^{1/3}$  is kept constant (Seiß et al., 2005). All simulations use mono-sized particles of radius  $R_p$ . The unperturbed ring patch (without the moonlet) has geometrical optical depth  $\tau_0$  and the box dimensions are  $2L_x \times 2L_y$ . The normal coefficient of restitution  $\varepsilon$  is mostly chosen to be constant, except for X12 and X13 where the Bridges et al. (1984) dependence on the impact velocity is used.  $N$  denotes the number of ring particles in the simulation box.

Simulation number	$R_{\text{moon}}$ (m)	$h$ (m)	$\rho_{\text{moon}}$ ( $\text{g cm}^{-3}$ )	$a_{\text{moon}}$ (km)	$R_p$ (m)	$\tau_0$	$\varepsilon$	$\Omega_z/\Omega$	$L_x$ (m)	$L_y$ (m)	$N$
C1	10	13.0	0.9	100,000	1.0	0.08	0.5	3.6	180	4000	72,000
C2	15	19.5	0.9	100,000	1.0	0.08	0.5	3.6	270	6000	162,000
C3	20	26.1	0.9	100,000	1.0	0.08	0.5	3.6	240	8000	190,000
C4	25	32.6	0.9	100,000	1.0	0.08	0.5	3.6	300	10,000	300,000
C5	30	39.1	0.9	100,000	1.0	0.08	0.5	3.6	360	12,000	432,000
C6	40	52.1	0.9	100,000	1.0	0.08	0.5	3.6	480	16,000	768,000
C7	55	71.7	0.9	100,000	1.0	0.08	0.5	3.6	660	22,000	1,450,000
D8	12	15.6	0.9	100,000	1.0	0.09	0.5	3.6	144	1728	28,000
D9	12	15.6	0.9	100,000	1.0	0.16	0.5	3.6	144	1728	50,000
D10	12	15.6	0.9	100,000	1.0	0.32	0.5	3.6	144	1728	100,000
X11	20	26.1	0.9	100,000	1.0	0.08	0.5	1.0	240	8840	216,000
X12	20	26.1	0.9	100,000	1.0	0.08	Bridges	1.0	240	8840	216,000
X13	20	29.6	0.6	130,000	1.67	0.5	Bridges	1.0	500	3000	344,406

in order to provide a good base for the comparison with the hydrodynamic propeller model. Table 2 shows the simulation labeling and parameters.

The core set of simulations (C1–C7) consists of runs for different moonlet radii ranging from 10 m to 55 m. We use a low optical depth of 0.08 so that simulations with large moonlets become computationally feasible. In order to reliably fit Eq. (53) to the tail of the azimuthal height decay, the simulations are made for a rather long azimuthal extent and the height decay is accelerated by an enhanced collision frequency (which is due to an enhanced vertical frequency  $\Omega_z$  of the particles<sup>5</sup>).

Additional simulations check the influence of different optical depths of the unperturbed ring (D8–D10, X13) and effects of the enhanced vertical frequency of the particles (C3, X11).

#### 4.1. Ratio of thermal velocity dispersion components

An important assumption of the hydrodynamic propeller model is that the asymptotic value of the velocity dispersion ratio  $c_z/c_x$  is established after a few collisions per particle, thus enabling the description of the propeller height decay with help of the granular temperature  $T$  and the equilibrium values  $(c_z/c_x)_{\text{eq}}$ .

Fig. 7 shows the evolution of the velocity dispersion ratio  $c_z/c_x$  in the propeller gap region determined from simulation C5 of a moonlet with  $R_{\text{moon}} = 30$  m. The azimuthal distance  $y$  to the moonlet is given in number of orbits it takes a ring particle with Keplerian orbital speed to get to that azimuthal position. The shown  $c_z/c_x$  values are radially averaged over the interval  $x \in [-2.7h, -2.0h]$  and the asymptotical ratio is emphasized by the thin gray horizontal line.

The evolution of  $c_z/c_x$  is characterized by the superposition of the moonlet-induced wake motion and the collisionally induced relaxation of the velocity dispersion ratio. Shortly after the encounter with the moonlet, the ratio  $c_z/c_x$  drops considerably to a value of about 0.2, supporting that the moonlet induces much more thermal motion in the ring plane than in vertical direction. The level of the asymptotic ratio is then reached quickly after less than half an orbit. Afterwards, the ratio  $c_z/c_x$  performs damped oscillations about the asymptotic value till it is reached after a few orbits downstream of the moonlet.

Adapted to the respective collision frequencies, these findings are confirmed by all other simulations for the gap as well as for the wake region. Thus, using a constant value  $(c_z/c_x)_{\text{eq}}$  for the fits

to the tails of the propeller height decay is justified fairly well. On the other hand, the maximal propeller heights are reached during the first orbits after the encounter with the moonlet, and because of the somewhat decreased velocity dispersion ratio  $c_z/c_x$  between the first and second orbit after the encounter with the moonlet, the propeller heights may be overestimated by about 20–25% in the hydrodynamic propeller model.

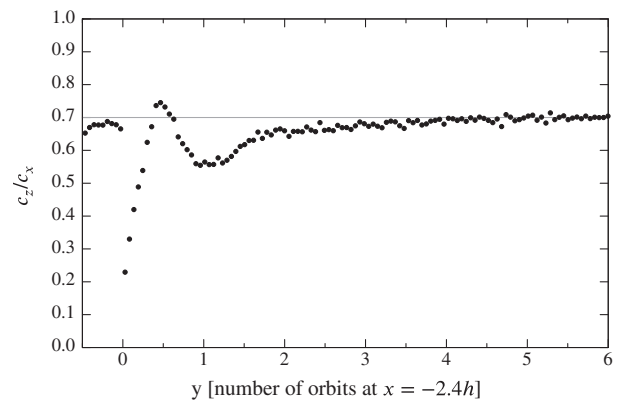
#### 4.2. Azimuthal height relaxation

Enhanced vertical frequencies lead to decreased ring heights (cf. Wisdom and Tremaine, 1988). To properly compare propeller heights between local box simulations with enhanced vertical frequencies and the hydrodynamical propeller model, we compensate for this effect of the enhanced vertical frequencies and calculate the propeller heights by

$$H = \frac{\Omega_z}{\Omega} \sqrt{3 \langle z^2 \rangle}. \quad (54)$$

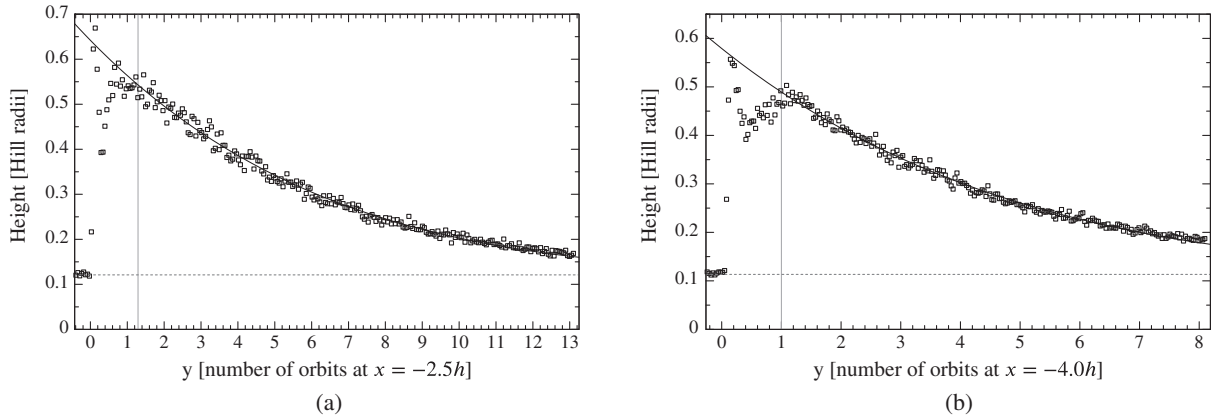
Although this relation is simplified (cf. Salo et al., 2001) and usually used for a steady state situation, our simulations without enhanced vertical frequencies, like X11, give similar maximal and averaged heights.

Fig. 8 shows the azimuthal evolution of the propeller height  $H$  at radial positions (a)  $x = -2.5h$  in the propeller gap region and (b)



**Fig. 7.** Azimuthal evolution of the velocity dispersion ratio  $c_z/c_x$  at radial position  $x = -2.4h$  in the propeller gap region, taken from simulation C5 (moonlet with 30 m radius). After a steep decline of  $c_z/c_x$  right after the scattering with the moonlet, the ratio reaches the asymptotic level (shown as faint gray horizontal line) after less than half an orbit and subsequently performs damped oscillations around that value.

<sup>5</sup> An enhanced vertical frequency of the particles is often used to describe the effect of the vertical self-gravity component (see e.g. Wisdom and Tremaine, 1988).



**Fig. 8.** Azimuthal evolution of the propeller height (compensated for the enhanced vertical frequencies for proper comparison with Section 3) at radial positions (a)  $x = -2.5h$  in the propeller gap region and (b)  $x = -4.0h$  in the propeller wake region, taken from simulation C5 (moonlet with 30 m radius). The dashed horizontal line marks the height of the unperturbed ring before the encounter with the moonlet. The vertical line labels the begin of the fit of Eq. (53) to the tail of the decaying height, which is shown as black solid line.

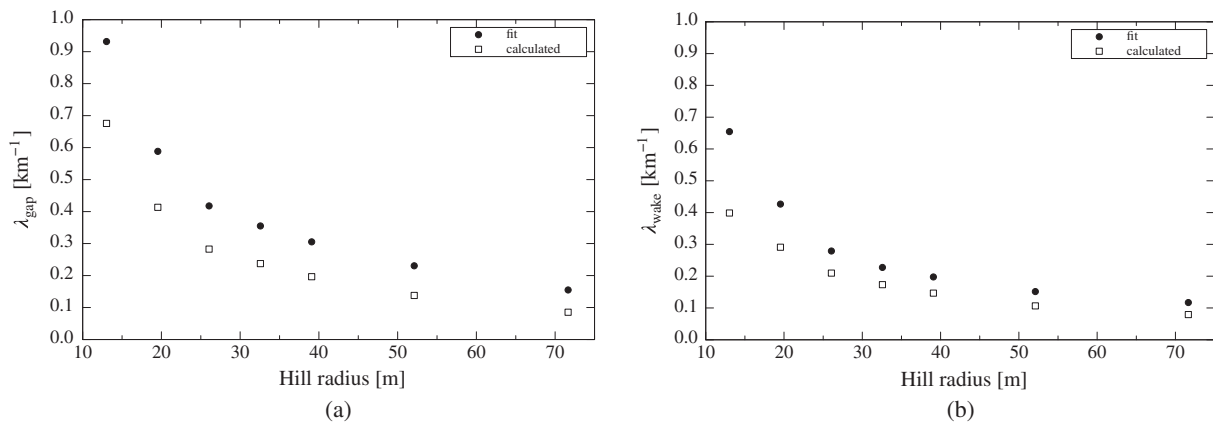


**Fig. 9.** Comparison of fitted and calculated values of the exponential decay constant  $\lambda$  for (a) the propeller gap region and (b) the propeller wake region for different moonlet sizes (simulations C1–C7). The filled circles mark values of  $\lambda$  fitted to Eq. (53), whereas the open squares are calculated with Eq. (55). The calculated values fit fairly well differing by 25–45% from the fitted ones.

$x = -4h$  in the propeller wake region for a moonlet with radius  $R_{\text{moon}} = 30$  m (simulation C5). The dashed horizontal line marks the height of the unperturbed ring before the encounter with the moonlet. The vertical line labels the point where we began the fit of Eq. (53) to the tail of the decaying height, which is shown as black solid line.

The exponential decay constants determined from these fits are  $\lambda_{\text{fit}} = 0.3 \text{ km}^{-1}$  in case of  $x = -2.5h$  and  $\lambda_{\text{fit}} = 0.23 \text{ km}^{-1}$  in case of  $x = -4h$ . In order to compare these values determined from simulations with enhanced vertical frequency with Eq. (49), we replace the optical depth  $\tau$  by the collision frequency  $\omega_c$

$$\lambda = \frac{2\omega_c(1 - \varepsilon^2)}{9\Omega|x|} - \frac{k_1(\omega_c/\Omega)}{|x|(1 + \frac{1}{9}(\omega_c/\Omega)^2)} \quad (55)$$

and calculate the collision frequency with  $\omega_c = 3\Omega_z\tau_{\text{eff}}$ , where we use an averaged value  $\tau_{\text{eff}}$  for the optical depth. For example,  $\tau_{\text{eff}} \approx 0.75\tau_0$  in the gap region and  $\tau_{\text{eff}} \approx 1.1\tau_0$  in the wake region of simulation C5 (moonlet with 30 m radius).

The values of the exponential decay constant calculated in that way are  $\lambda_{\text{calc}} = 0.16 \text{ km}^{-1}$  for  $x = -2.5h$  and  $\lambda_{\text{calc}} = 0.18 \text{ km}^{-1}$  for  $x = -4h$ , which differ by 47% and 22% from the ones determined from the fits. This difference might be partly due to the neglect

of heat conduction, which we expect to be of importance for small moonlets with radii of a few tens of meters, but which should be of minor importance for large moonlets like Blériot and Earhart with radii of a few hundred meters.

In Fig. 9, average exponential decay constants for different moonlet sizes (simulations C1–C7) are shown. We radially averaged the values of the propeller height over  $x \in [-3h, -1h]$  in the propeller gap region (Fig. 9a) and over  $x \in [-6h, -4h]$  in the propeller wake region (Fig. 9b). Filled circles denote values from fits to Eq. (53), whereas open squares denote values calculated from Eq. (55).

The calculated values agree fairly well with the fitted ones, differing by 25–45%. Furthermore, the calculated values are smaller which is expected for smaller moonlets like the ones we simulated due to the neglect of heat conduction.

These findings are confirmed by simulation X13 whose parameters are close to the situation in Saturn's A ring. We determined an exponential decay constant of  $\lambda_{\text{fit}} = 0.93 \text{ km}^{-1}$  for  $x = -2.4h$  from the fit and calculated an exponential decay constant of  $\lambda_{\text{calc}} = 0.62 \text{ km}^{-1}$  from Eq. (55), where we used  $\varepsilon = 0.4$  to approximate the Bridges et al. (1984) dependence of the restitution coefficient on the impact velocity. Here, the calculated value  $\lambda_{\text{calc}}$  differs by 34% from  $\lambda_{\text{fit}}$ , determined from the fit.

**Table 3**

Heights for different sized moonlets from simulations C1–C7. For proper comparison with the hydrodynamical propeller model, the heights are multiplied by  $\Omega_z/\Omega$ .  $H_{\max}$  is the maximal height at  $x = -2.0h$ .  $H_{\text{gap}}$  is the height radially averaged over the radial region  $x \in [-3h, -1h]$  and  $H_{\text{wake}}$  is the height radially averaged over the radial region  $x \in [-6h, -4h]$ .

$R_{\text{moon}}$ (m)	10	15	20	25	30	40	55
$H_{\max}$ (h)	0.78	0.74	0.72	0.71	0.68	0.67	0.65
$H_{\text{gap}}$ (h)	0.69	0.62	0.62	0.61	0.60	0.58	0.55
$H_{\text{wake}}$ (h)	0.57	0.51	0.48	0.48	0.47	0.45	0.43

### 4.3. Propeller heights

In the N-body simulations, the maximal propeller heights are reached in the propeller gap region at about  $x = -2h$ , as was the case in our model in Section 3. Table 3 shows propeller height values<sup>6</sup> for the simulations C1–C7 with different sized moonlets. Apart from the maximal height  $H_{\max}$ , taken at  $x = -2h$ , averaged heights are listed.  $H_{\text{gap}}$  is radially averaged over  $x \in [-3h, -1h]$  in the propeller gap region, and  $H_{\text{wake}}$  is radially averaged over  $x \in [-6h, -4h]$ , a region where moonlet wakes are of importance.

We find the difference between the height values of the propeller gap and wake regions to be less pronounced than they were in Fig. 6a. The gap averaged values from Table 3 are on average about 27% smaller than the ones determined from our model in Table 1. This is likely because the maximal propeller heights are reached during the first orbits after the encounter with the moonlet, where the velocity dispersion ratio  $c_z/c_x$  is somewhat decreased (cf. Section 4.1) which would explain the difference.

Therefore we use values determined from the local N-body simulations to estimate moonlet sizes from measured propeller heights. Maximal and averaged propeller heights are similar for simulations with and without enhanced vertical frequencies, if the heights of the former are calculated with Eq. (54) to compensate for the height decreasing effect of enhanced vertical frequencies. For definiteness, we employ a propeller height of  $0.65h$ , a value between  $H_{\max}$  and  $H_{\text{gap}}$  (cf. Table 3), to estimate moonlet sizes.

There seems to be a modest trend to smaller relative height values  $H/h$  for larger moonlets (see Table 3). This might be due to the fading influence of the initial velocity dispersion of the ring for increasing moonlet sizes (cf. Table 1).

We also analyzed simulations for higher optical depth. In simulations D8–D10, the geometrical optical depth was varied for a small moonlet with a radius of 12 m. Table 4 shows the maximal, gap averaged and wake averaged heights. The maximal height values are slightly higher than the ones from Table 3 and we suspect a modest trend to smaller gap and wake averaged height values with increasing optical depths.

Simulations made with the Bridges et al. (1984) dependence of the restitution coefficient on the impact velocity (X12 and X13) lead to smaller relative heights, for example, the gap averaged heights for X12 and X13 are  $0.51h$  and  $0.53h$ . On average, more energy is lost per collision, an approximate constant coefficient of restitution leading to these height values would be between  $\varepsilon = 0.3$  and  $\varepsilon = 0.4$ . The maximal height  $H_{\max}$  in simulation X12 is found to be about  $0.7h$ .

Concluding, we found a relation connecting propeller heights to moonlet sizes. Further, a fair agreement between the relaxation process in the hydrodynamic model and N-body simulations is found, enabling us to make predictions for large propeller moonlets, where N-body simulations are not feasible with common computational resources.

**Table 4**

Propeller heights for a moonlet with  $R_{\text{moon}} = 12$  m and different optical depths of the unperturbed ring (simulations D8–D10). For proper comparison with the hydrodynamical propeller model, the heights are multiplied by  $\Omega_z/\Omega$ .  $H_{\max}$  is the maximal height at  $x = -2.0h$ .  $H_{\text{gap}}$  is the height radially averaged over the radial region  $x \in [-3h, -1h]$  and  $H_{\text{wake}}$  is the height radially averaged over the radial region  $x \in [-6h, -4h]$ .

$\tau_0$	0.09	0.16	0.32
$H_{\max}$ (h)	0.78	0.80	0.84
$H_{\text{gap}}$ (h)	0.68	0.65	0.58
$H_{\text{wake}}$ (h)	0.57	0.49	0.43

## 5. Results and discussion

### 5.1. Maximal propeller heights

The gravitational interaction of the ring particles with a non-inclined moonlet alone is not sufficient to induce considerable vertical excursions of ring particles. However, the moonlet excites a substantial amount of thermal motion in the ring plane and subsequent collisions of ring particles are an efficient and quick mechanism to partly convert the lateral induced thermal motion into vertical motion.

The maximal propeller heights are reached in the propeller gap region around the radial position  $|x| = 2h$ . However, in case of the local N-body simulations, we find the difference between the height values of the propeller gap and wake regions to be less pronounced than they were in the hydrodynamical propeller model. The extended hydrodynamical propeller model predicts gap-averaged maximal heights of about 0.8–0.85 Hill radii, values which we find to be quite robust with respect to changes to the moonlet Hill radius. The local N-body simulations predict somewhat smaller values of about 0.5–0.7 Hill radii for the gap-averaged maximal heights.

The difference between the height predictions of the extended propeller model and the N-body simulations is dominated by the decreased velocity dispersion ratio  $c_z/c_x$  during the first few orbits downstream of the moonlet, in which the maximal propeller heights are reached. Additionally, the hydrodynamical propeller model neglects inelastic collisions in the scattering region. These inelastic collisions would reduce the energy of the ring particles, which might be especially relevant for ring particles which come close to the moonlet and gain, thereby, high eccentricities and inclinations. Furthermore, accretion and erosion of ring particles at the moonlet (Lewis and Stewart, 2009) are further processes which certainly can affect the propeller height.

For local N-body simulations with increasing optical depth we find a modest trend to smaller averaged heights in the gap and wake regions, deserving further investigation in the future. Furthermore, the effect of a particle size distribution on the maximal propeller heights is of great interest, though we leave it for future work.

Table 5 shows Hill radii of the four shadow-casting propellers estimated with the relation  $h = H/0.65$  of Section 4.3 and with propeller heights taken from Tiscareno et al. (2010). For comparison, Hill radii estimated from the radial propeller scaling are shown. These are calculated from  $\Delta r = (9 \pm 1)h$  relating the radial offset  $\Delta r$  of the leading and trailing propeller lobes to the moonlet's Hill radius  $h$  (Sremčević et al., 2007). We use radial offset values from Tiscareno et al. (2010), Fig. 2, which measure the radial offset of the bright propeller lobes in lit side images of Saturn's rings (labeled *Lit Side, Relative-Bright* in Tiscareno et al. (2010)).

The values of both approaches to estimate the Hill radius agree quite well for Blériot and Earhart. For Santos-Dumont, however, the Hill radius estimate calculated from the propeller height is 2.7 times smaller than the estimate calculated from the radial

<sup>6</sup> Propeller heights are compensated for the effects of enhanced vertical frequencies to properly compare them to our model of the vertical propeller height from Section 3.

**Table 5**

Hill radii for the four shadow casting propellers that were imaged by Cassini. Propeller height values are taken from Tiscareno et al. (2010) and the corresponding Hill radii are calculated from  $h = H/0.65$  from Section 4.3. For comparison, Hill radii calculated from the radial offset  $\Delta r$  of the leading and trailing propeller lobes are shown. Values of  $\Delta r$  are taken from Tiscareno et al. (2010) (from Fig. 2, labeled *Lit Side, Relative-Bright*) and the Hill radii are calculated from  $\Delta r = (9 \pm 1)h$  (Sremčević et al., 2007).

Propeller	Height (m)	Hill radius (from height) (m)	Hill radius (from radial scaling) (m)
Blériot	430	660	600 ± 80
Earhart	260	400	560 ± 80
116-006-A	160	250	–
Santos-Dumont	120	180	480 ± 60

offset of the propeller lobes, which is nevertheless on the same order of magnitude.

Estimates of the radius of Blériot range from 83 m, determined from UVIS measurements made during the occultation of  $\zeta$  Orionis (Baillié et al., 2013), to about 1 km, calculated from the radial propeller scaling with the relation  $\Delta r = 4h$  (Tiscareno et al., 2010). The UVIS measurement serves as a lower bound, because it is very unlikely that the propeller was scanned at the azimuthal position where its radial width was largest (Baillié et al., 2013). The size estimates from the propeller height, on the other hand, are in favor of interpreting the bright propeller lobes as being caused dominantly by the propeller wake region, confining Blériot's radius to less than 500 m. Further progress, with more precise estimates will require photometric modeling of the propeller structure along the lines presented in Halme et al. (2010).

## 5.2. Azimuthal relaxation of the propeller height

In our extended propeller model, the azimuthal relaxation of the propeller height is modeled by the disturbed balance of viscous heating and granular cooling using the hydrodynamical energy balance equation of the ring particle's thermal motion. This approach assumes that the velocity dispersion of the ring particles can be described by a scalar value. However, in a planetary ring the velocity dispersion is described by a tensor  $Tr\hat{\mathbf{T}}$  and the eigenvalues of this tensor are different in general, corresponding to different granular temperatures in different directions. Also, the lateral principal axes of the velocity dispersion tensor do generally not align with the radial and azimuthal direction, a fact which will have to be addressed in future model extensions.

On the other hand, the local equilibrium ratios of the diagonal elements of the velocity dispersion tensor,  $(c_y/c_x)_{eq}$  and  $(c_z/c_x)_{eq}$ , are established quickly after a few collisions per particle (Section 4.1, Hämeen-Anttila and Lukkari, 1980; Hämeen-Anttila and Salo, 1993). Thus, after these equilibrium ratios are established, for our purposes the velocity dispersion can be described with a scalar value, i.e. with the granular temperature  $T = Tr\hat{\mathbf{T}}/3$ , and with the equilibrium values of  $c_y/c_x$  and  $c_z/c_x$ .

Because of the vertically inefficient gravitational interaction of the moonlet with the ring particles, we have restricted our description to the ring plane and assumed a Gaussian vertical mass distribution (cf. Simon and Jenkins, 1994; Schmidt et al., 1999). The vertical propeller structure is then completely described by the granular ring temperature  $T$  and by  $(c_y/c_x)_{eq}$  and  $(c_z/c_x)_{eq}$ .

We have neglected the temperature decrease due to heat conduction, based on the grounds that the relaxation of the ring temperature due to the disturbed balance of viscous heating and granular cooling is much faster for large propeller moonlets. For a moonlet with a 300 m Hill radius the exponential decay of the granular temperature takes about 20 orbits, whereas stochastic

diffusion processes, like the gap-closing or heat conduction, operate on the mass diffusion timescale  $t_{diff} = (\Delta r)^2/\nu$ . The gap closing, for example, takes hundreds of orbits for a moonlet with 300 m Hill radius (Spahn and Sremčević, 2000; Sremčević et al., 2002). However, heat conduction as well as viscous diffusion could become important for small moonlets, an issue to be addressed in future work.

In the extended propeller model, we further used a ring viscosity  $\nu = \nu_\star + \nu_l$ , where  $\nu_\star$  is assumed to be temperature independent on timescales relevant to the exponential decay of the granular temperature. The local viscosity  $\nu_l$ , on the other hand, is assumed to be proportional to the granular temperature (Goldreich and Tremaine, 1978). This assumed form of the temperature dependence of  $\nu$  is a simplification, but allows an analytical solution (Eqs. (48) and (53)) in case of large moonlets, for which we expect the timescale of the exponential temperature decay and the timescale of the mass diffusion to clearly separate.

The temperature independent part  $\nu_\star$  can accommodate a part  $\nu_{nl}$  which is due to the momentum transfer over particle diameters in collisions as well as a part  $\nu_{grav}$  which is due to gravitational torques exerted by self-gravity wakes (Araki and Tremaine, 1986; Daisaka et al., 2001). A more general model of the kinematic viscosity would be

$$\nu = \nu_0 \left( \frac{\Sigma}{\Sigma_0} \right)^\beta \left( \frac{r}{a_0} \right)^\gamma \left( \frac{T}{T_0} \right)^\alpha \quad (56)$$

(e.g. Spahn et al., 2000), which, however, will make it most likely necessary to solve the energy balance equation numerically.

We fitted our analytical solution (53) to results of local N-body simulations, which were made with simulation boxes of rather large azimuthal extent (showing, for example, about 16 orbits downstream of the moonlet at radial distance  $|x| = 2h$ ). The simulations were made for rather small moonlets (radii between 10 m and 55 m) due to limited computational resources. Considering the neglect of heat conduction in the derivation of our analytical solution (53), which we expect to be of greater importance for small moonlets, calculated values of the exponential decay constant agree fairly well with the values from the fits to the simulation results. The calculated values differ by 25–45% from the fitted ones, which holds for values radially averaged over the gap region as well as for values radially averaged over the wake region. This agreement is remarkable considering that we used steady state relations for the viscosity, the collision frequency and the energy loss due to inelastic collisions to describe the highly perturbed ring around the moonlet.

Two days after Saturn's equinox, Cassini took two images showing the Earhart propeller casting a pronounced shadow, 350 km long, offering the opportunity to witness how the ring height, excited by the propeller moonlet, relaxes to an equilibrium state. By assuming that the azimuthal evolution of the propeller height vertically limits the light-blocking region of the propeller, Hoffmann et al. (2013) determined the exponential cooling constant of the propeller height relaxation from the shape of the shadow cast by Earhart (Fig. 10). Using Eq. (53) to describe the propeller height, the best match between the projected curve and the shadow boundary was found for  $\lambda = 0.07 \pm 0.02 \text{ km}^{-1}$ , leading to a propeller height halving after about 20 km.

Using Eq. (55), the above value of the exponential cooling constant suggests<sup>7</sup> a collision frequency of  $\omega_c/\Omega = 1.0$  in the propeller gap region at the radial position  $|x| = 2h$ , corresponding to about 6 collisions per particle per orbit. In the wake region at the radial

<sup>7</sup> We used  $\varepsilon = 0.4$  and  $k_1 = 0.15$  (Stewart et al., 1984) for the estimation of the collision frequency with Eq. (55).

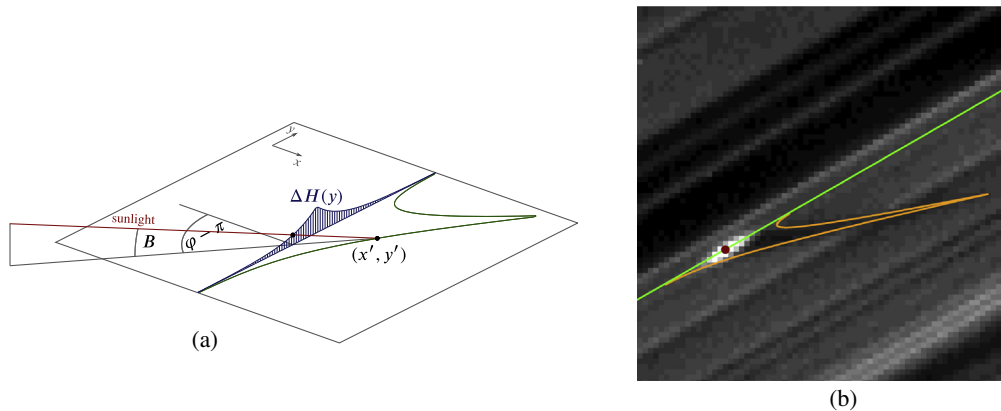


**Fig. 10.** (a) Calculation of the shadow boundary by projecting the height difference  $\Delta H(y)$  between propeller and surrounding ring material onto the ring plane, using the elevation angle of the sunlight  $B$  and the longitude of the Sun  $\varphi$ . (b) Image of the propeller Earhart near Saturn's equinox (N1628846513), taken by Cassini's narrow angle camera on August 13, 2009. The shadow cast by the propeller is 350 km long. The azimuthal evolution of the height difference between propeller and surrounding ring material is projected into the image as an estimate of the shadow boundary using Eq. (53). An exponential cooling constant of  $\lambda = 0.07 \pm 0.02 \text{ km}^{-1}$  was found (Hoffmann et al., 2013). From Eq. (55) we estimate a collision frequency of  $\omega_c/\Omega = 1.0$  in the propeller gap region and  $\omega_c/\Omega = 1.7$  in the propeller wake region. This corresponds to about 6 collisions per particle per orbit in the gap region and about 11 collisions per particle per orbit in the wake region.

position  $|x| = 4.5h$ , we find a collision frequency of  $\omega_c/\Omega = 1.7$  or about 11 collisions per particle per orbit.

Using  $\omega_c = 3\Omega\tau$ , an often-used estimate of the collision frequency for dilute rings (cf. Schmidt et al., 2009; Shu and Stewart, 1985), we find optical depths of  $\tau = 0.3$  for the gap region and  $\tau = 0.6$  for the wake region. These values are quite consistent with mean optical depths in the gap and wake regions of a propeller in the A ring.

On a sub-km scale, Saturn's A ring is populated by self-gravity wakes, transient trailing density enhancements, which are the result of the opposing gravitational accretion of ring particles and Keplerian shear. The radial spacing between self-gravity wakes is close to Toomre's critical wavelength  $\lambda_{\text{crit}}$  (Toomre, 1964), which is about 50–100 m in Saturn's A ring, depending on the surface mass density and the distance to Saturn.

The hydrodynamical propeller model of Section 2.3 should be a good coarse-grained description of the propeller relaxation, as long as the Hill radius  $h$  of the moonlet (the characteristic radial length scale of the propeller) is much larger than the critical wavelength  $\lambda_{\text{crit}}$ , and parameters like the ring viscosity and the velocity dispersion are chosen accordingly.

For the propellers Earhart and Blériot, with Hill radii of several hundred meters,  $h \gg \lambda_{\text{crit}}$  constitutes a fair assumption. Also, the induced radial velocity dispersion in the vertical excited region of big propellers will be much larger than the critical radial velocity dispersion below which self-gravity wakes form. However, for smaller propellers, with Hill radii similar to the critical wavelength, a more detailed description will be important, which is subsequent work in progress.

Another quite challenging future task arises from the physical similarities between planetary rings and protoplanetary disks around young stars (Burns and Cuzzi, 2006). Although protoplanetary disks are composed of a turbulent gas-dust mixture in contrast to the icy particles in Saturn's rings, the similarities are nevertheless manifold. In that analogy the propeller moonlets in Saturn's rings correspond to planetary embryos in protoplanetary disks and future work should address the prediction of extended structures in those disks carved in by planetary embryos.

## Acknowledgments

We like to thank two anonymous reviewers for providing helpful comments on an earlier version of this manuscript and

we thank Jürgen Schmidt for very useful and encouraging discussions. We kindly acknowledge the efforts of the Cassini ISS team in the design and operation of the ISS instrument. This work was supported by Deutsche Forschungsgemeinschaft (Sp 384/24-2; 25-1), by the Academy of Finland and by Deutsches Zentrum für Luft- und Raumfahrt (OH 1401).

## References

- Araki, S., Tremaine, S., 1986. The dynamics of dense particle disks. *Icarus* 65, 83–109.
- Artymowicz, P., 2006. Planetary systems. *Am. Inst. Physics Conf. Ser.* 843, 3–34.
- Baillié, K. et al., 2013. Meter-sized moonlet population in Saturn's C ring and Cassini Division. *Astron. J.* 145, 171.
- Bridges, F.G., Hatzes, A., Lin, D.N.C., 1984. Structure, stability and evolution of Saturn's rings. *Nature* 309, 333–335.
- Burns, J.A., Cuzzi, J.N.C., 2006. Our local astrophysical laboratory. *Science* 312, 1753–1755.
- Colwell, J.E. et al., 2009. The structure of Saturn's rings. In: Doherty, M.K. et al. (Eds.), *Saturn from Cassini-Huygens*. Springer, Dordrecht, pp. 375–412.
- Daisaka, H., Tanaka, H., Ida, S., 2001. Viscosity in a dense planetary ring with self-gravitating particles. *Icarus* 154, 296–312.
- Goldreich, P., Tremaine, S., 1978. The velocity dispersion in Saturn's rings. *Icarus* 34, 227–239.
- Halme, V.-P. et al., 2010. Dynamical and photometric simulations of propeller features in Saturn's A ring. In: *AAS/Division for Planetary Sciences Meeting Abstracts, Bulletin of the American Astronomical Society*, vol. 42.
- Hämeen-Anttila, K.A., Lukkari, J., 1980. Numerical simulations of collisions in Keplerian systems. *Astrophys. Space Sci.* 71, 475–497.
- Hämeen-Anttila, K.A., Salo, H., 1993. Generalized theory of impacts in particulate systems. *Earth, Moon, Planets* 62, 47–84.
- Henon, M., 1981. A simple model of Saturn's rings. *Nature* 293, 33–35.
- Hénon, M., Petit, J.-M., 1986. Series expansion for encounter-type solutions of Hill's problem. *Celest. Mech.* 38, 67–100.
- Hill, G.W., 1878. Researches in the lunar theory. *Am. J. Math.* 1, 5–26, 129–147, 245–260.
- Hoffmann, H., Seiß, M., Spahn, F., 2013. Vertical relaxation of a moonlet propeller in Saturn's A ring. *Astrophys. J.* 765, L4.
- Ida, S., Makino, J., 1992. N-body simulation of gravitational interaction between planetesimals and a protoplanet. I – Velocity distribution of planetesimals. *Icarus* 96, 107–120.
- Lewis, M.C., Stewart, G.R., 2009. Features around embedded moonlets in Saturn's rings: The role of self-gravity and particle size distributions. *Icarus* 199, 387–412.
- Lissauer, J.J., 1993. Planet formation. *Ann. Rev. Astron. Astrophys.* 31, 129–174.
- Lissauer, J.J., Shu, F.H., Cuzzi, J.N., 1981. Moonlets in Saturn's rings. *Nature* 292, 707–711.
- Morishima, R., Salo, H., 2006. Simulations of dense planetary rings. IV. Spinning self-gravitating particles with size distribution. *Icarus* 181, 272–291.
- Ohtsuki, K., Emori, H., 2000. Local N-body simulations for the distribution and evolution of particle velocities in planetary rings. *Astron. J.* 119, 403–416.
- Papaloizou, J.C.B. et al., 2007. Disk-planet interactions during planet formation. *Protostars Planets V*, 655–668.
- Petit, J.-M., Hénon, M., 1986. Satellite encounters. *Icarus* 66, 536–555.

- Petit, J.-M., Hénon, M., 1987. A numerical simulation of planetary rings. I – Binary encounters. *Astron. Astrophys.* 173, 389–404.
- Petit, J.-M., Hénon, M., 1988. A numerical simulation of planetary rings. III – Mass segregation, ring confinement, and gap formation. *Astron. Astrophys.* 199, 343–356.
- Press, W.H. et al., 1992. *Numerical Recipes in C*, second ed. Cambridge University Press.
- Salo, H., 1991. Numerical simulations of dense collisional systems. *Icarus* 90, 254–270.
- Salo, H., 1995. Simulations of dense planetary rings. III. Self-gravitating identical particles. *Icarus* 117, 287–312.
- Salo, H., Schmidt, J., Spahn, F., 2001. Viscous overstability in Saturn's B ring. I. Direct simulations and measurement of transport coefficients. *Icarus* 153, 295–315.
- Schmidt, J. et al., 1999. Vertical distribution of temperature and density in a planetary ring. *Astron. Astrophys.* 345, 646–652.
- Schmidt, J. et al., 2001. Viscous overstability in Saturn's B-ring. II. Hydrodynamic theory and comparison to simulations. *Icarus* 153, 316–331.
- Schmidt, J. et al., 2009. Dynamics in Saturn's rings. In: Doherty, M.K. et al. (Eds.), *Saturn from Cassini-Huygens*. Springer, Dordrecht, pp. 413–548.
- Seiß, M. et al., 2005. Structures induced by small moonlets in Saturn's rings: Implications for the Cassini mission. *Geophys. Res. Lett.* 32. <http://dx.doi.org/10.1029/2005GL022506>.
- Seiß, M., Spahn, F., 2011. Hydrodynamics of Saturn's dense rings. *Math. Model. Nat. Phenom.* 6 (4), 191–218.
- Showalter, M.R. et al., 1986. Satellite "Wakes" and the orbit of the Encke Gap moonlet. *Icarus* 66, 297–323.
- Shu, F.H., Stewart, G.R., 1985. The collisional dynamics of particulate disks. *Icarus* 62, 360–383.
- Simon, V., Jenkins, J.T., 1994. On the vertical structure of dilute planetary rings. *Icarus* 110, 109–116.
- Spahn, F., 1987. Scattering properties of a moonlet (satellite) embedded in a particle ring: Application to the rings of Saturn. *Icarus* 71, 69–77.
- Spahn, F., Sremčević, M., 2000. Density patterns induced by small moonlets in Saturn's rings? *Astron. Astrophys.* 358, 368–372.
- Spahn, F., Wiebicke, H.J., 1989. Long-term gravitational influence of moonlets in planetary rings. *Icarus* 77, 124–134.
- Spahn, F. et al., 2000. Note: Stability analysis of a Keplerian disk of granular grains: Influence of thermal diffusion. *Icarus* 145, 657–660.
- Spahn, F., Scholl, H., Hertzsch, J.-M., 1994. Structures in planetary rings caused by embedded moonlets. *Icarus* 111, 514–535.
- Spahn, F., Schwarz, U., Kurths, J., 1997. Clustering of granular assemblies with temperature dependent restitution under Keplerian differential rotation. *Phys. Rev. Lett.* 78, 1596–1599.
- Sremčević, M. et al., 2007. A belt of moonlets in Saturn's A ring. *Nature* 449, 1019–1021.
- Sremčević, M. et al., 2008. Density waves in Saturn's rings: Non-linear dispersion and Moon libration effects. *Bullet. Am. Astron. Soc.* 40, 430.
- Sremčević, M., Spahn, F., Duschl, W.J., 2002. Density structures in perturbed thin cold discs. *Mon. Not. Roy. Astron. Soc.* 337, 1139–1152.
- Stewart, G.R., Lin, D.N.C., Bodenheimer, P., 1984. Collision-induced transport processes in planetary rings. In: Greenberg, R., Brahic, A. (Eds.), *Planetary Rings*. Univ. of Arizona Press, Tucson, pp. 447–512.
- Tiscareno, M.S. et al., 2006. 100-metre-diameter moonlets in Saturn's A ring from observations of "propeller" structures. *Nature* 440, 648–652.
- Tiscareno, M.S. et al., 2007. Cassini imaging of Saturn's rings. II. A wavelet technique for analysis of density waves and other radial structure in the rings. *Icarus* 189, 14–34.
- Tiscareno, M.S. et al., 2008. The population of propellers in Saturn's A ring. *Astron. J.* 135, 1083–1091.
- Tiscareno, M.S. et al., 2010. Physical characteristics and non-Keplerian orbital Motion of "Propeller" Moons embedded in Saturn's rings. *Astrophys. J.* 718, L92–L96.
- Toomre, A., 1964. On the gravitational stability of a disk of stars. *Astrophys. J.* 139, 1217–1238.
- Wisdom, J., Tremaine, S., 1988. Local simulations of planetary rings. *Astron. J.* 95, 925–940.